

Check for updates

Multi-Ion Doping Controlled CEI Formation in Structurally-Stable High-Energy Monoclinic-Phase NASICON Cathodes for Sodium-Ion Batteries

Sharad Dnyanu Pinjari, Vignesh Mahalingam, Purandas Mudavath, Malavika Aarayil, Tasdique Arman, Ipsita Pal, Dipan Kundu, Raghavan Ranganathan,* Ashok Kumar Nanjundan,* and Rohit Ranganathan Gaddam*

Overcoming the energy density limitations of sodium-ion batteries (NIBs) requires innovative strategies to optimize cathode materials. While entropy-engineering through multi-ion doping has shown promise, previous efforts in polyanion-type cathodes are confined to conventional (pyro)phosphate-based systems. Here, it is reported for the first time a entropy-engineered NASICON-type cathode, NaFe_{1.8}(MnCrAlZnIn)_{0.2}(PO₄) (MoO₄)₂ (NFM'PM20), stabilized in a rare monoclinic P2/c phase via solid-state reaction. This entropy design enables robust cathode-electrolyte interphase (CEI) formation, mitigates lattice strain, and reduces the bandgap, collectively facilitating reversible 2.6 Na⁺ storage with an exceptional energy density of 315.62 Wh kg⁻¹. The NFM'PM20 cathode demonstrates outstanding cycling stability (92.2% capacity retention after 500 cycles at 5C) and ultra-long cycle life exceeding 2000 cycles. Mechanistic investigations via in situ X-ray diffraction confirm a strain-accommodating solid-solution reaction mechanism with minimal volume change (≈4.5%). At the same time, electron paramagnetic resonance and magnetic susceptibility measurements demonstrate enhanced Fe spin-states, which improve electrontransport. Ex-situ transmission electron microscope images reveal a thin and stable CEI layer. Density functional theory calculations elucidate the atomic-scale advantages, including optimized Na⁺ migration pathways with 0.45 eV lower diffusion barriers and enhanced interfacial charge transfer kinetics. The NFM'PM20 cathode represents a transformative advancement for developing practical high-energy-density NIBs.

1. Introduction

The global push toward sustainable renewable energy has heightened the demand for high-performance energy storage systems. Although lithium-ion batteries (LIBs) have dominated the market for the past decade, their dependence on scarce minerals and vulnerability to geopolitical instability pose major supply chain risks. Sodium-ion batteries (NIBs) offer a promising, cost-effective alternative due to sodium's abundance; however, their widespread adoption hinges on overcoming a critical challenge: developing a high-energy cathode material.

Among leading sodium-ion cathode materials, NASICON-type structures have shown promise but currently rely on costly metals, such as vanadium. [3b,4] To improve cost efficiency, researchers are exploring earth-abundant alternatives, such as iron (Fe), as redox-active sites. [5] NASICONs primarily crystallize in a rhombohedral phase (R-3c), though a monoclinic phase (C2/c, P2/c) can also form. [6] Iron-based (pyro)phosphates are among the most studied low-cost NASICON cathodes; however, they suffer from

S. D. Pinjari, P. Mudavath, M. Aarayil, R. R. Gaddam Department of Chemical Engineering Indian Institute of Science Education and Research-Bhopal Bhopal, Madhya Pradesh 462066, India E-mail: rohitg@iiserb.ac.in

The ORCID identification number(s) for the author(s) of this article can be found under https://doi.org/10.1002/adfm.202517539

© 2025 The Author(s). Advanced Functional Materials published by Wiley-VCH GmbH. This is an open access article under the terms of the Creative Commons Attribution-NonCommercial-NoDerivs License, which permits use and distribution in any medium, provided the original work is properly cited, the use is non-commercial and no modifications or adaptations are made.

DOI: 10.1002/adfm.202517539

V. Mahalingam, T. Arman, R. Ranganathan Department of Materials Engineering Indian Institute of Technology Gandhinagar Palaj, Gandhinagar, Gujarat 382355, India E-mail: rraghay@iiton.ac.in

E-mail: rraghav@iitgn.ac.in

I. Pal, D. Kundu LBRI School of Chemical Engineering UNSW Sydney Kensington, NSW 2052, Australia

A. K. Nanjundan Centre for Future Materials and the School of Engineering University of Southern Queensland

Brisbane, QLD 4300, Australia E-mail: ashok.nanjundan@unisq.edu.au





www.afm-journal.de

poor electrical conductivity, limited Na⁺ uptake, severe voltage hysteresis, and high polarization, all of which hinder energy density.^[7] Recent strategies to mitigate these issues include anion substitution by introducing highly electronegative polyanions to enhance redox activity and electronic transport,^[8] as well as cation doping to stabilize the crystal structure.^[9]

A potential approach to further optimize these materials is an entropy engineering design, which incorporates multiple elements in near-equimolar ratios to form a single-phase solid solution.[10] This approach leverages the configurational entropy to simultaneously achieve three critical improvements: 1) suppression of phase segregation, 2) mitigation of lattice strain during electrochemical cycling, and 3) enhancement of ionic/electronic conductivity.[11] Recent research highlights the potential of entropic modifications, where Zhang et al. developed Na₄Fe_{2.85} (Ni, Co, Mn, Cu, and Mg)_{0.03}(PO₄)₂P₂O₇, achieving 122 mAh g⁻¹ at 0.1 C,^[7a] while subsequent optimization through Zn substitution yielded even greater performance (165 Wh kg⁻¹ in full-cell configurations).[12] Wang et al. and Liu et al., further investigated the entropy engineering strategy, demonstrating superior rate capability and cycling stability across various entropy-stabilized NASICON cathodes.[5b,13] Despite these advances, two fundamental limitations remain unaddressed: i) persistent structural degradation during extended cycling, and ii) the unexplored potential of multi-ion doping in NASICON-type polyanionic frameworks beyond conventional (pyro)phosphate

Therefore, for the present work, we have chosen a unique polyanionic NASICON framework with the formula NaFe₂(PO₄)(MoO₄)₂ (NFPM) as a cathode. This material incorporates [MoO₄]2⁻ a transition metal oxide as the polyanion, which offers three key advantages: 1) its larger ionic size facilitates enhanced Na⁺ transport, 2) its metallic character (derived from Mo 3d orbitals) significantly improves electronic conductivity, and 3) its balanced inductive effect promotes faster ionic transport. In NFPM, the Fe sites are partially substituted with a tailored combination of five transition and post-transition metals (Mn, Cr, Al, Zn, In, denoted as M'). This multi-ion substitution at Fe sites effectively mitigates voltage decay by minimizing overpotential. Density functional theory (DFT) calculations and galvanostatic intermittent titration technique (GITT) reveal that entropy engineering strategy optimizes the crystal structure, reduces the energy bandgap to enhance electrical conductivity, and facilitates Na+ transport through expanded diffusion channels with lowered energy barriers. In situ X-ray diffraction (XRD) further confirms a single-phase solid-solution reaction mechanism during Na⁺ insertion/deinsertion, with exceptionally low lattice strain (0.0091) and minimal volume change (4.5%), demonstrating remarkable structural stability.

The optimized NaFe_{1.8}(MnCrAlZnIn)_{0.2}(PO₄)(MoO₄)₂ (NFM'PM20) cathode exhibits outstanding electrochemical performance, achieving a high specific discharge capacity of 125.21 mAh g⁻¹ at 0.1 C and a remarkable energy density of 315.62 Wh kg⁻¹. Notably, NFM'PM20 exhibits excellent rate capability (82 mAh g⁻¹ at 1 C) and long-term cycling stability, retaining 84.30% capacity after 400 cycles at 0.1 C, 83.46% after 500 cycles at 2 C, and 65.85% after 2000 cycles at 5 C. These enhancements are systematically corroborated through ex-situ X-ray photoelectron spectroscopy (XPS), ex-situ field emission

scanning electron microscopy (FESEM), high-resolution transmission electron microscopy (HR-TEM), in situ electrochemical impedance spectroscopy (EIS), and distribution of relaxation time (DRT) analysis. Collectively, these findings underscore the transformative potential of entropy engineering in NASI-CON cathodes, offering fundamental insights into structural stabilization and electrochemical optimization. This work paves the way for sodium-iron phosphomolybdate cathodes as high-performance, cost-effective candidates for next-generation NIBs.

2. Results and Discussion

The NFM'PM powder samples are prepared via a straightforward solid-state reaction method. The synthesis route includes two major steps: uniform mixing of precursors (first step) followed by sintering (second step) at high temperature (**Figure 1**). A detailed synthesis process is described in the Experimental Section (see Supporting Information). To obtain a more stable single-phase crystal framework without defects, a mixed-valent dopant of Mn²⁺, Cr³⁺, Al³⁺, Zn²⁺, and In³⁺ was selected. The multi-ion doped entropy engineering concept has been extensively utilized in battery research since its introduction in the field of alloys. [14] In statistical thermodynamics, the configurational entropy (ΔS_{config}), enthalpy of mixing (ΔH_{mix}), and Gibbs free energy of mixing (ΔG_{mix}) can be defined as: [12]

$$\Delta S_{config} = -R \left(\sum_{i=0}^{n} x_i ln x_i \right)$$
 (1)

$$\Delta G_{\text{mix}} = \Delta H_{\text{mix}} - T\Delta S_{\text{mix}}$$
 (2)

$$\Delta H_{\text{mix}} = \sum_{i,j,i\neq j} x_i x_j \Omega_{ij} = \sum_{i,j,i\neq j} 4x_i x_j \Delta H_{\text{mix},ij}$$
(3)

where x_i , x_i represent the mole fraction of i^{th} and j^{th} species, R is the universal gas constant, T represents the temperature in Kelvin, Ωij denotes the regular solution interaction energy, and $\Delta H_{mix,ij}$ is the enthalpy of mixing for a binary alloy solution.^[15] Additionally, ΔS_{config} is crucial for maintaining the thermodynamic stability of the solid-solution phase, as it minimizes ΔG_{mix} . [16] The calculated results (Figure 2a,b) using the above relations represent trade-offs between the ideal charge storage capacity and ΔS_{config} at varying dopant concentrations (i.e., x). The ΔG_{mix} decreases with increasing dopant concentration and reaches its minimum in the composition range of $x \approx 0.1 - 0.2$, indicating enhanced thermodynamic stability in this region (Note: For each dopant, the mole fraction (x_i) is 0.02 summing up to a total "x" of 0.2 moles). At x=0.20, the ΔS_{config} of NFM'PM20 increased by 4.06 J mol⁻¹ K⁻¹, while ΔG_{mix} was minimized to 136.6 J mol⁻¹ at room temperature. Hence, entropy-informed multi-ion substitution may generate a greater potential interaction combination and provide distinct energy storage properties.

For material design, $\Delta S_{config} > 1.5R$, $1.0R \le \Delta S_{config} \le 1.5R$, and $\Delta S_{config} < 1.0R$ are classified as high entropy (HE), medium entropy (ME), and low entropy (LE) materials, respectively. [17] It is worth noting that this work primarily focuses on the LE and ME, as the HE material preparation requires multiple trial-and-error

16163028, 0, Downloaded from https://advanced.onlinelibrary.wiley.com/doi/10.1002/adfm.202517539 by Raghavan Rar

- Indian Institute of Technology Gandhinagar , Wiley Online Library on [23/09/2025]. See the Terms and Conditions (https:

and-conditions) on Wiley Online Library for rules of use; OA articles are governed by the applicable Creative Commons License

SCIENCE NEWS

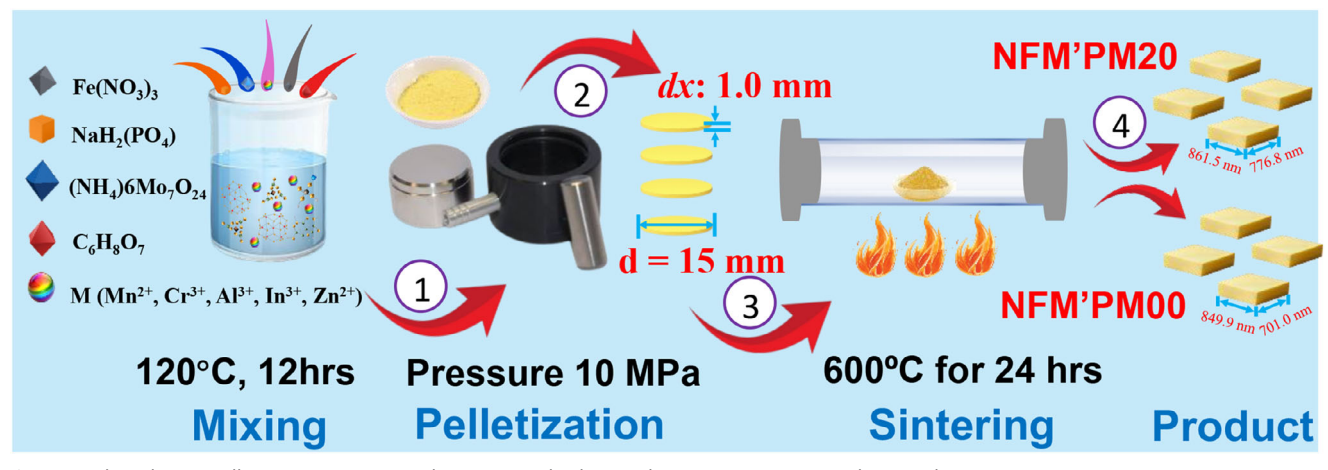


Figure 1. The schematic illustration represents the steps involved in synthesizing NFM'PM powder samples.

attempts, making the process time-consuming and thereby constraining related research. [4a,7a] From Figure S1a,b (Supporting Information), NFM'PM10, NFM'PM20, and NFM'PM30 belong to LE, while NFM'PM40 is ME (the detailed calculations are provided in Note \$1, Supporting Information and Figure \$1, Supporting Information below).

2.1. Structural and Morphological Characterization

To confirm the formation of NASICONs post-synthesis, XRD patterns of all NFM'PM samples were analyzed using Rietveld refinement (Figure 2c; Figure S2a-d, Supporting Information). The accurate fitting of all diffraction peaks confirms that the material forms a monoclinic NASICON-type structure with a P2/c space group. Furthermore, all repeated individual XRD patterns along with sharp peaks corroborate the high phase purity and crystalline nature of the resulting material (Figure 2d). These results strongly suggest that the dopants selectively occupy the stoichiometrically substituted Fe octahedral sites, while molybdenum (Mo) preferentially resides in the tetrahedral coordination environment, as expected under the applied synthesis conditions. If Mo were to occupy octahedral sites or replace Fe, it would likely induce the formation of secondary phases or introduce additional diffraction features, none of which were observed. Additionally, the magnified XRD peaks (right-hand side of Figure 2d) exhibit a successive shift toward lower angles with increasing dopant concentration, which is predominantly linked to disparities in the ionic radii of the Mn²⁺, 0.80 Å; Cr³⁺, 0.62 Å; Al³⁺, 0.54 Å; Zn²⁺, 0.80 Å; In³⁺, 0.81 Å compared to Fe³⁺, 0.64 Å. Comprehensive structural data, including atomic coordinates, Wyckoff positions, site occupancy, and unit cell parameters for NFM'PM samples derived from Rietveld refinement, are summarized in Tables S1-S5 (Supporting Information). The structural analysis reveals that the lattice parameters of NFM'PM00 (a = 12.7125 Å, b = 8.9775 Å,c = 9.1470 Å) are notably smaller than those of NFM'PM20 (a = 12.8054 Å, b = 9.0180 Å, c = 9.1836 Å). Also, the unit cell volumes of NFM'PM00 and NFM'PM20 are calculated to be 1043.63 and 1060.15 Å³, respectively, suggesting that the incorporation of multi-ion dopant regulates the crystal structure. The increasing trend in lattice parameters with dopant concentration further verifies structural expansion induced by the introduction of dopants (Figure S2e, Supporting Information). The average bond distance of Fe/M and oxygen (d_{Fe/M-O}) for NFM'PM20 (Figure 2e) is 1.9952 Å, which is higher than NFM'PM00 (i.e., $d_{\text{Fe},O} = 1.9835$ Å). The elongation of the Fe/M—O bond and expansion of the lattice parameters in NFM'PM20 suggest an enhanced Na+ diffusion pathway that potentially lowers the energy activation barrier and improves electrode kinetics. The 3D structural models of NFM'PM00 and NFM'PM20 are shown in Figure 2e. At the atomic level, the crystal framework of NFM'PM has two distinct "lantern units". The first unit consists of two Fe/MO₆ octahedra and two PO₄ tetrahedra, along with a single MoO₆ tetrahedron. The second unit is composed of two Fe/MO6 octahedra coordinated with three MoO₄ tetrahedra. These octahedral and tetrahedral units are interconnected via shared oxygen atoms. The stacking of "lantern units" in a nearly parallel configuration forms a robust 3D open framework with large interstitial sites that can enhance Na+ storage.

To get more insight into the elemental composition and chemical valence states of NFM'PM00 and NFM'PM20, X-ray photoelectron spectroscopy (XPS) was employed. The full scan XPS spectra (Figure 3a; Figure S3a, Supporting Information), acquired in the 0-1200 eV binding energy range, show peaks of Na 1s, Zn 2p, Fe 2p, Mn 2p, Cr 2p, O 1s, In 3d, C 1s, Mo 3d, P 2p, and Al 2p. The well-defined signals of the dopants serve as direct evidence of the successful substitution of the five elements into the NFM'PM20 cathode. The deconvoluted Fe 2p spectra have two prominent peaks (Figure 3b; Figure S3b, Supporting Information) at \approx 711.61 eV (Fe $2p_{3/2}$) and 725.61 eV (Fe $2p_{1/2}$), confirming the existence of iron in Fe³⁺. [18] Additionally, a satellite peak was observed ≈717.61 eV. [9a,11b] The Mo 3d spectra (Figure 3c; Figure S3c, Supporting Information) show two characteristic peaks at 232.80 and 235.94 eV associated with Mo $3d_{5/2}$ and Mo $3d_{3/2}$, respectively. The oxidation states of the dopants must be accurately assessed to understand their potential participation in electrochemical reactions. In 3d, it shows the peaks at 445.33 eV (In $3d_{5/2}$), and 452.87 eV (In $3d_{3/2}$), which correspond to the 3+ valence state of In (Figure 3d).[19] The peaks are located at 642.18 eV (Mn $2p_{3/2}$) and 654.43 eV (Mn $2p_{1/2}$) in the Mn 2p spectrum

of Technology Gandhinagar, Wiley Online Library on [23/09/2025]. See the Term

are governed by the applicable Creative

www.afm-journal.de

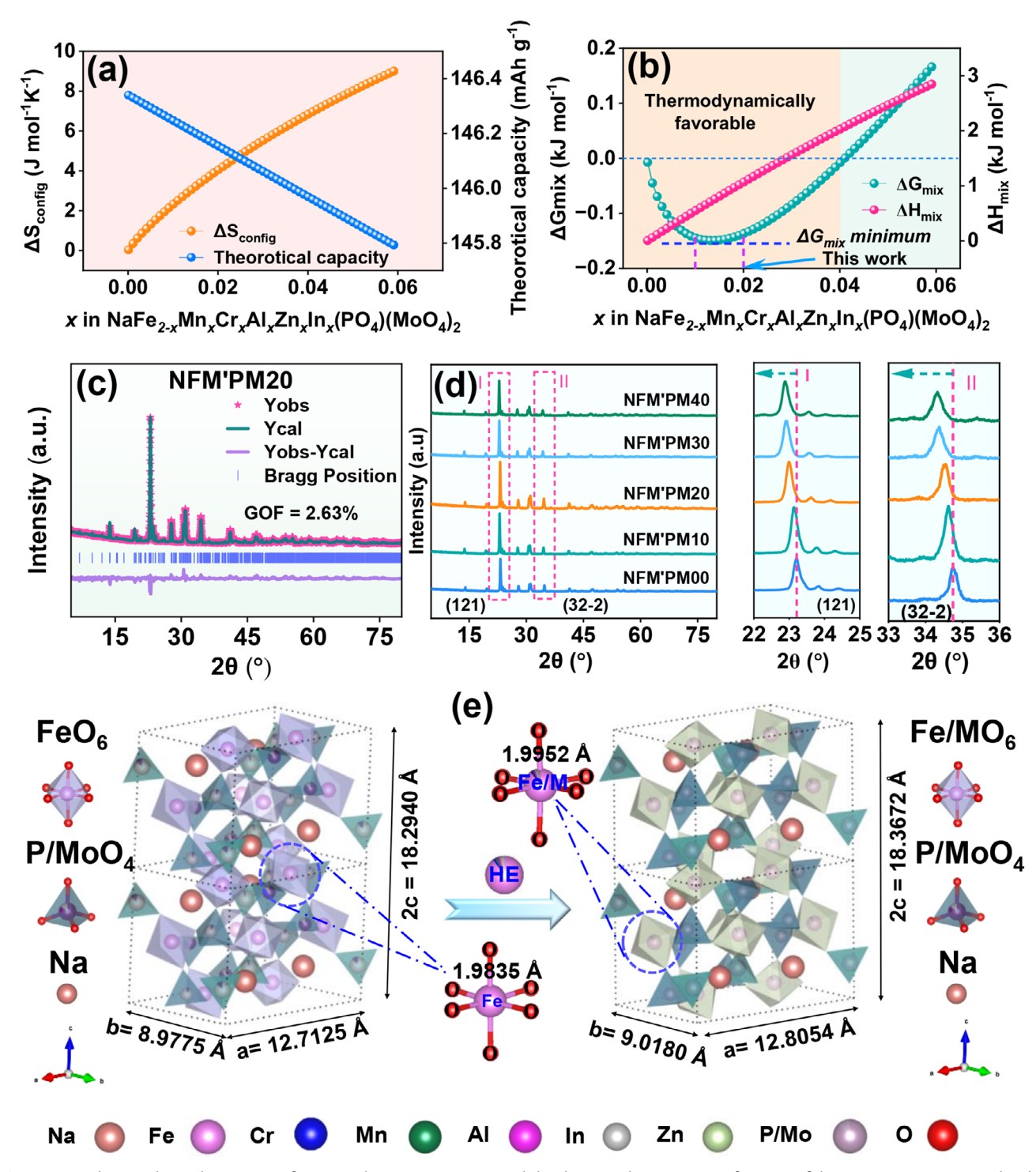


Figure 2. a) The correlation between configurational entropy (ΔS_{config}) and the theoretical capacity as a function of dopant concentration (x); b) The relationship among ΔG_{mix} , ΔH_{mix} , and x at room temperature; c) Rietveld refinement profile of NFM'PM20; d) X-ray diffraction (XRD) patterns of all samples with a magnified view of selected peaks; e) Schematic illustration of multi-ion dopants on the crystal structure of NFM'PM00.

(Figure 3e), indicating the 2+ oxidation state of Mn.^[13] Zn 2p exhibited two peaks at \approx 1022.52 eV (Zn 2p_{3/2}) and \approx 1045.62 eV (Zn 2p_{1/2}), verifying the divalent state of Zn (Figure 3f).^[20] The Cr 2p spectrum exhibits two bands at 758.07 eV (Cr 2p_{3/2}) and 587.59 eV (Cr 2p_{3/2}), which can be attributed to Cr³⁺ (Figure 3g).^[19] Sim-

ilarly, for Al 2p, the peaks \approx 74.65 eV (Al 2p_{3/2}) and 76.51 eV (Al 2p_{1/2}) confirm the trivalent state of Al (Figure 3h).^[21] Furthermore, the C 1s exhibit different peaks (Figures S3d,h, Supporting Information) corresponding to C—C (284.88 eV), C—O (286.49 eV), and O—C=O (288.96 eV). ^[22] The pronounced C—C

16163028, 0, Downloaded from https://advanced.onlinelibrary.wiley.com/doi/10.1002/adfm.202517539 by Raghavan Ranga

nathan - Indian Institute of Technology Gandhinagar, Wiley Online Library on [23/09/2025]. See the Terms

litions) on Wiley Online Library for rules of use; OA articles

are governed by the applicable Creative Commons License

www.afm-journal.de

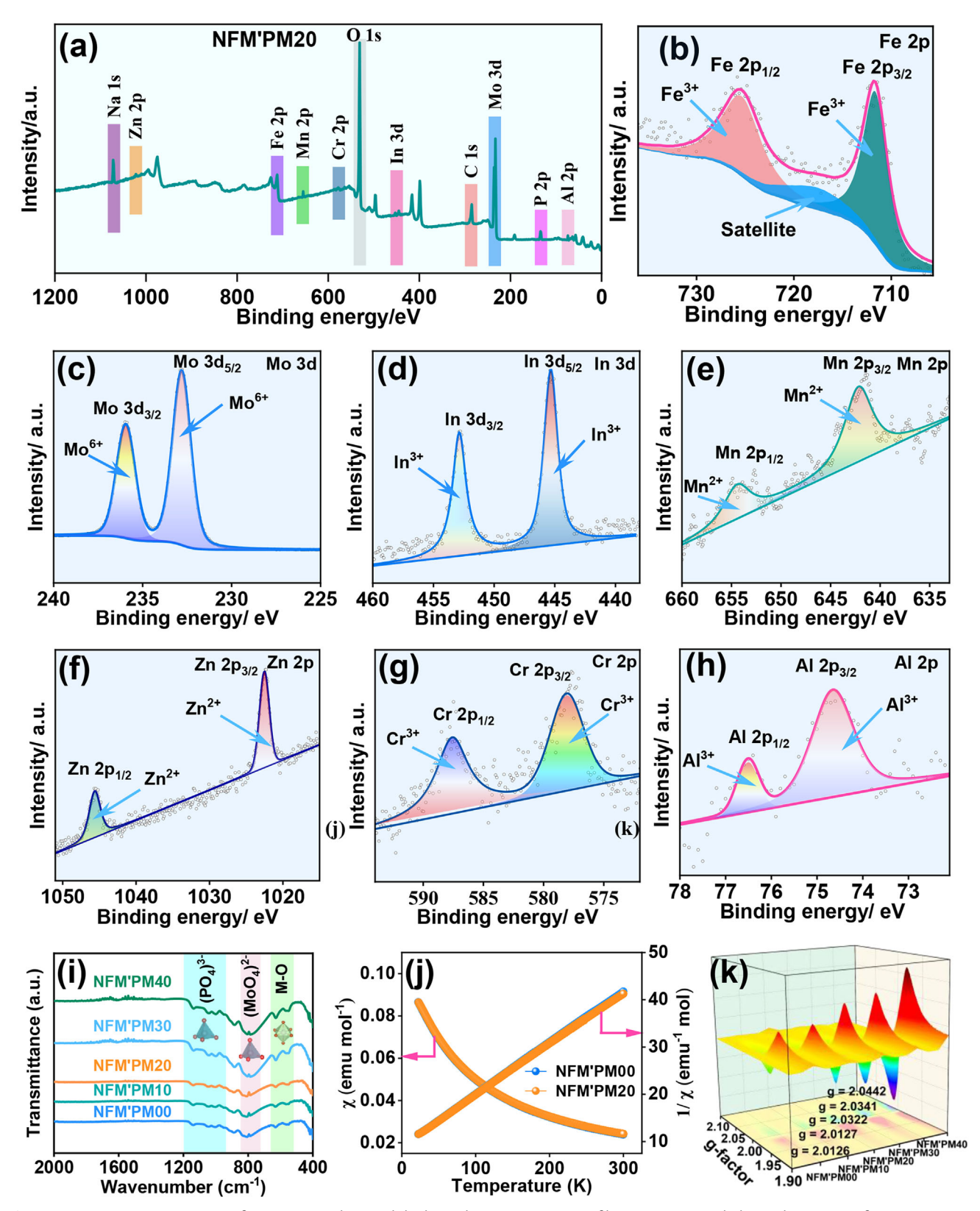


Figure 3. a) XPS survey spectrum of NFM'PM20, along with high-resolution XPS spectra of b) Fe 2p, c) Mo 3d, d) In 3d, e) Mn 2p, f) Zn 2p, g) Cr 2p, and h) Al 2p; i) FTIR curves of all NFM'PM samples; j) Magnetization (M-H) curves of NFM'PM00 and NFM'PM20; and k) EPR spectra of all samples.





www.afm-journal.de

peaks observed in NFM'PM00 and NFM'PM20 indicate the deposition of an amorphous carbon layer on the particle surfaces, derived from citric acid as the carbon source. The P 2p band at 133.54 eV (P 2p_{3/2}) signifies the presence of phosphorus in the (PO4)3 state (Figure S3e,i, Supporting Information). The five peaks of O 1s placed at 531.10, 530.41, 532.97, 531.98, and 535.34 eV are representative of the O-M, O-P, O-C=O, O-C, and adsorbed H₂O bonding (Figure S3f,j, Supporting Information).[23] These results demonstrate the effective incorporation of the carbon network and (PO4)3- polyanion group into samples. The Na 1s spectra exhibit a broad peak centered ≈1072.1 eV (Figure S3g,k, Supporting Information). Fouriertransform infrared (FTIR) (Figure 3i) and Raman spectroscopy (Figure S4a, Supporting Information) were further employed to analyze the structural characteristics of samples. The peaks near 559.10 and 630.72 cm⁻¹ correspond to the stretching vibration of Fe/M' - O (here M' is Mn, Cr, Al, Zn, and In).[24] A series of peaks ≈ 999.12 , ≈ 1050.12 , and ≈ 1136.15 cm⁻¹ represent the O-P-O (bending) and P-O (stretching) vibrations of the (PO₄)3⁻¹ tetrahedron.^[25] Further, a peak ≈785.02 cm⁻¹ suggests the presence of the (MoO₄)2⁻ polyanion group in the structure. [26] The Raman peaks observed for NFM'PM00 and NFM'PM20 within the spectral range of 234 – 536 cm⁻¹ correspond to the symmetric and antisymmetric bending vibrational modes (O-Mo-O) of the (MoO₄)2 (Figure S4a, Supporting Information). Additionally, the peaks detected within the $780-970~\text{cm}^{-1}$ range are indicative of vibrational modes of the Mo-O bond in the MoO₄ tetrahedron.^[27] Nitrogen sorption analysis was employed to elucidate the surface characteristics of the material, which in turn have a profound impact on charge transport across the electrode. The NFM'PM00 sample exhibited a Brunauer-Emmett-Teller (BET) specific surface area of 0.7364 m² g⁻¹ (Figure S4b, Supporting Information), which is significantly lower than that of NFM'PM20 (2.2816 m² g⁻¹, Figure S4c, Supporting Information). Also, the Barrett-Joyner-Halenda (BJH) pore size of NFM'PM20 (4.6161 nm) was observed to be smaller than that of NFM'PM00 (4.7907 nm). The increased specific surface area signifies a greater abundance of active sites, while the narrower pore size distribution enables full electrolyte penetration within the NFM'PM20 cathode. Such structural optimization through multi-ion dopants can effectively facilitate the rapid transport of Na⁺, thereby improving the electrochemical performance of the cathode material.^[28] The thermogravimetric (TG) analysis of all prepared samples confirms thermal stability up to 700 °C, indicating that the cathode material can endure high temperatures without significant decomposition (Figure S4d, Supporting Information).

Apart from the microstructure of the sample, electronic and magnetic properties dictate the electrochemical performance of the cathode. Temperature-dependent magnetic susceptibility (M-T) and electron paramagnetic resonance (EPR) were used to investigate the enhanced spin states of NFM'PM post-doping. M-T measurements revealed a Curie-Weiss paramagnetic behavior for both NFM'PM00 and NFM'PM20 within the temperature range of 50 to 300 K. When plotted, $1/\chi$ versus T reveals a line with a lower slope for NFM'PM20 as compared to the pristine sample, indicative of enhanced paramagnetism post-doping (Figure 3j). EPR measurements reveal a positive shift following multi-ion doping, indicating an enhanced g-value (Figure 3k). The g-factor,

which offers insights into the electron's spin state, is affected by the angular momentum of the free electrons. Notably, an increase in g-value post-doing, i.e., 2.0126, 2.0127, 2.0322, 2.0341, and 2.0442 of NFM'PM00, NFM'PM10, NFM'PM20, NFM'PM30, and NFM'PM40, respectively, further aligns with observations via M-T measurements of an enhanced spin state. The direct consequence of the improvement in the spin state can be visualized as increased electrical conductivity in the doped samples. The average electrical conductivity values determined using the twopoint probe method, for NFM'PM00, NFM'PM10, NFM'PM20, NFM'PM30, and NFM'PM40 are 1.30×10^{-9} , 2.06×10^{-9} , 2.69×10^{-9} 10^{-9} , 4.00×10^{-9} , and 6.37×10^{-9} S cm⁻¹, respectively (Figure S5, Supporting Information). To further validate the enhancement in electrical conductivity obtained through multi-ion doping, the ultraviolet diffuse reflectance spectroscopy (UV-DRS) technique was utilized. The optical bandgap of the NFM'PM00 and NFM'PM20 cathodes was determined using the Kubelka-Munk equation (detailed calculations and corresponding plots are presented in Note S2 and Figure S6a,c, Supporting Information). The estimated bandgap of NFM'PM00 was 2.57 eV, which is higher than the 2.41 eV measured for NFM'PM20 (Figures S6b,d, Supporting Information). The reduced bandgap of the optimized sample effectively lowers the energy barrier for electron transport, resulting in enhanced electronic and ionic kinetics of the material.

The morphological characteristics, including particle size, shape, crystallinity, and lattice fringes, of the NFM'PM00 and NFM'PM20 samples were analyzed using FESEM and HRTEM. The FESEM images of NFM'PM00 (Figure 4a-c) exhibit the agglomeration of cuboid-shaped particles. Conversely, the introduction of multi-ion dopants significantly reduces particle coalescence in NFM'PM20 (Figure 4h-j), resulting in a nearly cubic morphology. HRTEM images further illustrate these morphological differences, where NFM'PM00 cuboids appear as rectangles (Figure 4d), whereas NFM'PM20 exhibits nearly squareshaped particles (Figure 4k,l). The HRTEM images show that the NFM'PM00 particle is coated with a thick carbon layer of 5 – 7 nm (Figure 4e), whereas the NFM'PM20 particle is coated with a thin and uniform carbon layer of 3 – 6 nm (Figure 4m). A thin carbon layer effectively mitigates particle agglomeration by preventing direct particle-to-particle contact, ensuring uniform distribution, and enhancing electron transport across the cathode material. Furthermore, both samples exhibit well-defined lattice fringes, with a d-spacing of 0.6293 nm for NFM'PM00 (Figure 4f,g) and 0.7148 nm for NFM'PM20 (Figure 4n,o), both corresponding to the same (110) plane. The higher d-spacing of NFM'PM20 compared to NFM'PM00 further validates the XRD observations, indicating possible lattice expansion influenced by the incorporation of dopants. The sharp diffraction spots observed in the selected area electron diffraction SAED patterns of NFM'PM00 (inset of Figure 4e) and NFM'PM20 (inset of Figure 4m) further confirm a long-range ordered structure. The elemental mapping of the samples (Figures S7a-h and S8a-l, Supporting Information) shows a uniform distribution of the elements in both materials and indicates the presence of dopants in NFM'PM20. Additionally, the FESEM-EDX spectra (Figure S7i,m, Supporting Information) verify the presence of elements in nearly stoichiometric proportions. Furthermore, the higher dopant concentration notably influences the morphology of NFM'PM10,



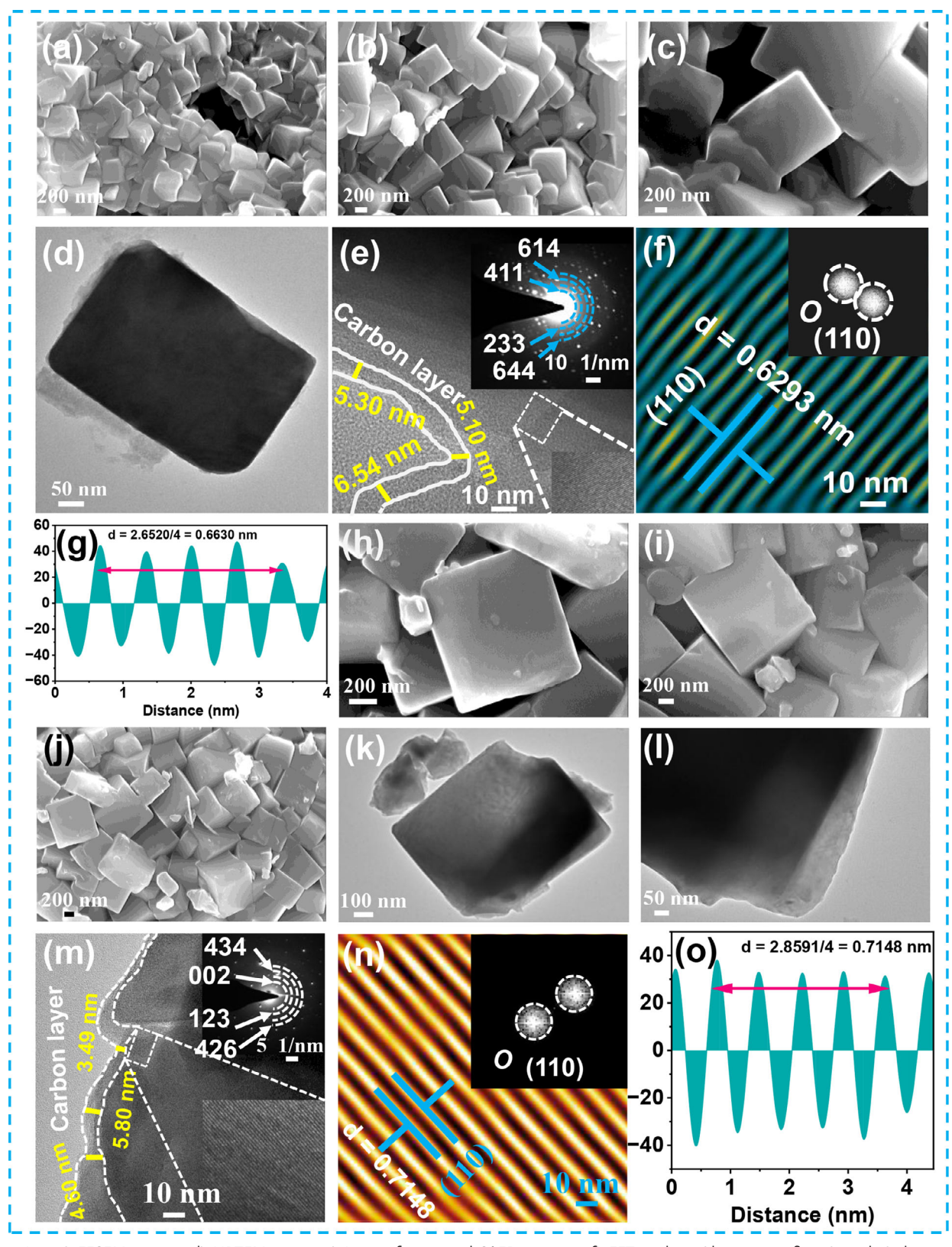


Figure 4. a—c) FESEM images, d) HRTEM image, e) Lattice fringes and SAED patterns, f) FFT analysis (the inset in figure), and g) d-spacing of NFM'PM00; similarly, h—j) FESEM images k,l) HRTEM images, m) Lattice fringes, and SAED patterns, n) FFT analysis (the inset in figure), and o) d-spacing of NFM'PM20 sample.





www.afm-journal.de

NFM'PM30, and NFM'PM40, as shown in Figure S9a-c (Supporting Information).

2.2. Sodium-Ion Storage Behavior in NFM'PM

As discussed in the earlier section, modulating the $\Delta S_{\textit{config}}$ of the electrode material can effectively alter the structural properties, which directly influence its electrochemical performance. The galvanostatic charge/discharge (GCD) test was performed on all NFM'PM samples in a half-cell configuration, using sodium metal as the anode. All GCD measurements were performed by first discharging from the open-circuit voltage (OCV). The second-cycle GCD profiles of the samples were recorded in the voltage range of 1.6-3.8 V at 0.1 C (Figure 5a). It can be seen that the entropy-engineered cathodes demonstrate an enhanced Na+ storage capacity compared to their pristine counterpart. In particular, NFM'PM00 exhibits a specific discharge capacity of 101.19 mAh g^{-1} , NFM'PM10 of 113.73 mAh g^{-1} , NFM'PM20 of 125.21 mAh g⁻¹, NFM'PM30 of 111.82 mAh g^{-1} , and NFM'PM40 of 109.56 mAh g^{-1} . Furthermore, to explore the trend of voltage versus capacity profiles, the initial 100-cycle charge/discharge profiles are shown in Figure 5b,c, and Figure S10a-c (Supporting Information) for NFM'PM00, NFM'PM10, NFM'PM20, NFM'PM30, and NFM'PM40, respectively. Notably, similar charge/discharge profiles observed across all the samples suggest that entropy-engineering does not alter the charge storage mechanism of the materials. In the initial 20 cycles, NFM'PM00 exhibits higher capacity decay compared to NFM'PM20, possibly due to the formation of a thicker and more unstable CEI layer on the surface, resulting in larger irreversible capacity loss at the beginning. However, after 100 cycles, the NFM'PM00, NFM'PM10, NFM'PM20, NFM'PM30, and NFM'PM40 deliver a discharge-specific capacity of 88.60, 98.78, 109.41, 92.88, and 87.20 mAh g⁻¹, respectively. The optimized NFM'PM20 shows the highest discharge-specific capacity even after 100 cycles. The charge/discharge profiles of all samples at different currents are shown in Figure 5d and Figure S10d-g (Supporting Information).

To gain deeper insights into the impact of the multi-ion dopant, the rate capability of all samples was evaluated by varying C-rates from 0.1 C to 5 C (Figure 5e; Figure S10h, Supporting Information). The discharge capacities of NFM'PM20 at varying C-rates of 0.1, 0.2, 0.5, 1, 2, 3, 4, and 5 C are 129.09, 114.21, 102.36, 82.61, 70.47, 58.36, 48.79, and 39.38 mAh g⁻¹, respectively. Notably, these values are higher than those of NFM'PM00, which shows discharge capacities of 101.34, 92.80, 79.30, 64.60, 47.28, 38.35, 35.14, and 30 mAh g⁻¹ at the corresponding C-rates, emphasizing the superior rate performance of NFM'PM20. Even at a high rate of 5 C, NFM'PM20 maintains a higher capacity of 39.38 mAh g⁻¹, which is 30% higher than that of NFM'PM00. Furthermore, upon reinstating the charge-discharge rate to 0.5 C, NFM'PM20 demonstrates a reversible discharge capacity of 116.48 mAh g⁻¹. Despite dynamic changes in C-rates after every 5 cycles, the NFM'PM20 still exhibits a plateau voltage profile with a polarization degree much lower than all the other samples. The results suggest that the entropy-engineering strategy in NFM'PM plays a crucial role in enhancing Na⁺ diffusion kinetics, thereby enabling improved rate capability and fast charging performance.

Life-cycle studies on NFM'PM cathodes were evaluated via GCD tests at C-rates of 0.1 C, 0.2 C, 1 C, 2 C, and 5 C. At a low current rate of 0.1 C. after 300 cycles. NFM'PM20 delivers a specific capacity of 91 mAh g^{-1} , with a capacity retention of 73.3% and an energy density of 227.5 Wh kg⁻¹, which is higher than the NFM'PM00 (72 mAh g⁻¹, 69.0% retention, and 180.0 Wh kg⁻¹) (Figure 5f,g). Likewise, NFM'PM10, NFM'PM30, and NFM'PM40 exhibit capacity retention of 65.96%, 70.85%, and 72.31%, with corresponding energy densities of 185.62 Wh kg^{-1} , 191.32 Wh kg^{-1} , and 183.36 Wh kg^{-1} , respectively (Figure S11a-c, Supporting Information). At 0.2 C, (Figure S13a,b, Supporting Information), NFM'PM20 shows a capacity of 90 mAh g⁻¹ with 70.1% retention after 350 cycles, whereas NFM'PM00 retains 62.9% of its capacity (70 mAh g⁻¹). The corresponding GCD profiles and differential capacity plot (dQ/dV versus V) over 100 cycles are shown in Figure S12 (Supporting Information). Also, at a higher current rate of 1 C, NFM'PM20 demonstrates superior electrochemical performance compared to NFM'PM00, delivering a capacity of 70.39 mAh g⁻¹ with 84.30% retention over 400 cycles, significantly higher than the 41.33 mAh g⁻¹ capacity and 60.96% retention of NFM'PM00 (Figure 5h,i). It is worth noting that, the capacity fluctuation observed in Figure 5h during long-term cycling can be attributed to the dynamics of the electrode-electrolyte interface and the progressive formation of a CEI, as evidenced by our ex-situ TEM and in- situ EIS analysis (discussed below). Furthermore, at 2 C, the capacity retention for NFM'PM00 (after 400 cycles), NFM'PM10, NFM'PM20, NFM'PM30, and NFM'PM40 after 800 cycles is 72.34%, 62.14%, 73.76%, 60.37%, and 40.24%, respectively (Figures \$14a-c,\$15a, and S16a, Supporting Information). At a high current rate of 5 C, NFM'PM00 exhibits a capacity retention of 86.45%, while NFM'PM20 demonstrates superior stability, retaining 92.20% of its capacity over 500 cycles and 65.85% over 2000 cycles (Figures S15b and S16b, Supporting Information). Notably, the performance degradation observed in NFM'PM30 and NFM'PM40 can be primarily attributed to excessive dopant incorporation at the redox-active Fe sites. This over-doping reduces the overall Fe content, thereby limiting the availability of Fe²⁺/Fe³⁺ redox couples essential for charge compensation. Furthermore, high dopant concentrations may introduce structural distortion and narrow Na⁺ diffusion channels, thereby hindering the ion transport kinetics. This is corroborated by EIS analyses (discussed below), which show the higher charge transfer resistance (TableS7, Supporting Information) for NFM'PM30 and NFM'PM40 compared to NFM'PM20. Overall, the optimized NFM'PM20 cathode material, developed using the entropy-engineering strategy, exhibits significant improvements in reversible Na+ storage capacity, long-term cycling stability, and rate capability. Additionally, to clearly elucidate the role of the (MoO₄)2⁻ polyanion in charge-storage performance, we synthesized the NASICON-type $Na_3Fe_2(PO_4)_3$ (NFP), by replacing the $(MoO_4)2^{-1}$ polyanion and adjusting the stoichiometry of the NFPM cathode, following the synthesis method reported in the literature. [29] The electrochemical performance, including charge/discharge capacity and cycling stability, is presented in Figure S17 (Supporting Information) alongside NFM'PM00. The results reveal that NFM'PM00 exhibits superior electrochemical behavior, highlighting the critical benefits of incorporating (MoO₄)²⁻ as a polyanion in the NA-SICON framework.

16163028, Q. Downloaded from https://advanced.onlinelibrary.wiley.com/doi/10.1002/adfm.202517539 by Raghavan Ranganathan - Indian Institute of Technology Gandhinagar , Wiley Online Library on [23/09/2025]. See the Term

on Wiley Online Library for rules of use; OA articles are governed by the applicable Creative

www.afm-journal.de

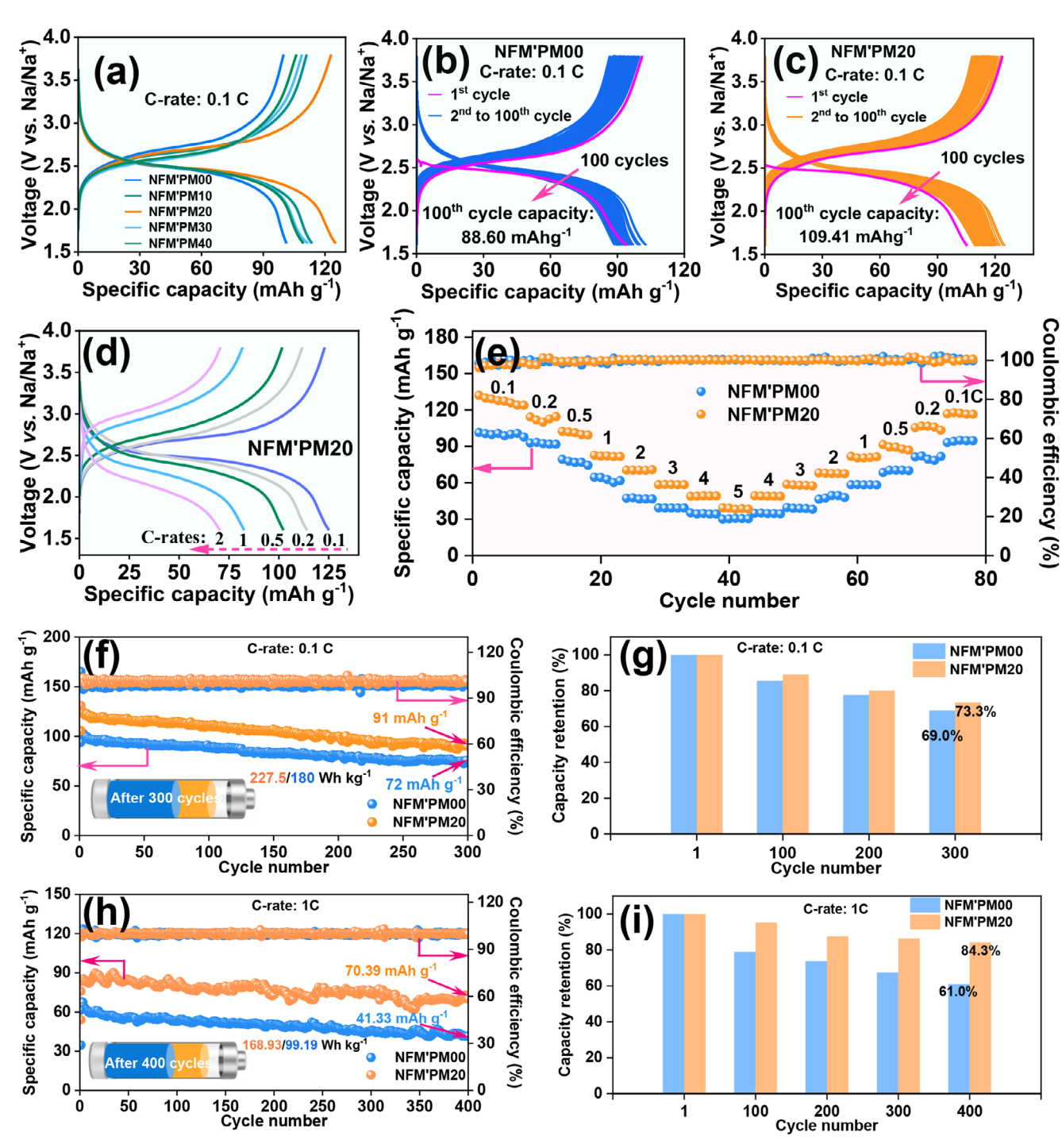


Figure 5. a) The GCD profiles of all NFM'PM samples during the second cycle, along with the initial 100-cycle GCD curves of b) NFM'PM00, and c) NFM'PM20 at a current rate of 0.1C; d) GCD curves of NFM'PM20 recorded at various C-rates; e) Rate capability performance evaluated over a range of C-rates from 0.1C to 5C; f,h) Long-term cycling stability and g,i) Corresponding capacity retention over different cycle numbers at 0.1C, and 1C, respectively.

2.3. Mechanism of Charge-Storage in NFM'PM

To further elucidate the effect of entropy-engineering strategy on the charge storage mechanism and electrode reaction kinetics, cyclic voltammetry (CV) tests were performed in a similar voltage range of 1.6 - 3.8 V versus Na/Na⁺. The cyclic voltammograms (CVs) of all samples were recorded at a scan rate of 0.15 mV s⁻¹ (Figure S18a–e, Supporting Information). The profile shows a pair of oxidation/reduction peaks and a voltage separation (Δ V) of 2.89/2.35 V; 0.54 V (NFM'PM00), 2.87/2.35 V; 0.52 V



www.afm-journal.de

(NFM'PM10), 2.81/2.36 V; 0.45 V (NFM'PM20), 2.75/2.38 V; 0.37 V (NFM'PM30), and 2.77/2.33 V; 0.44 V (NFM'PM40). The observed oxidation/reduction peaks are attributed to the Fe^{2+}/Fe^{3+} redox couple. The sharper peaks with a minimized ΔV obtained post-doping reflect the reduced degree of polarization, superior reaction reversibility, and enhanced electrochemical kinetics. This improvement is closely associated with enhanced ionic and electronic conductivity, ultimately contributing to the better electrochemical performance of cathode materials.^[30] To demonstrate the dynamics and Na⁺ kinetics of the electrodes, CV tests were performed at various scan rates from 0.10 to 0.30 mV s⁻¹ (Figure 6a,d; Figure S19a-g, Supporting Information, first column). All samples exhibit a similar shift in redox peaks with increasing scan rate, indicating typical Na⁺ storage behavior during the (de)insertion process. In particular, NFM'PM00 exhibits the $\Delta V \approx 0.46 \text{ V}$ (0.1 mV s⁻¹), and $\Delta V \approx 0.63 \text{ V}$ (0.30 mV s⁻¹), which are higher than the $\Delta V \approx 0.37 \text{ V}$ (0.1 mV s⁻¹) and $\Delta V \approx$ 0.61 V (0.30 mV s⁻¹) of NFM'PM20. This suggests that even at higher sweep rates, NFM'PM20 experiences lower polarization, resulting in improved rate capability during charge/discharge at high C-rates. Also, the monotonic shift in redox peaks with increasing scan rates indicates the occurrence of a quasi-reversible reaction of NFM'PM cathodes. According to the relation between the peak current (i_p) and sweep rate (v) $(i_p = av^b)$, Note S3, Supporting Information), the slope linearly fitted $log(i_n)$ versus log(v)gives the b-values (Figure \$20b-n, middle column). The calculated b-values (Figure S20c-o, Supporting Information, last column) for all samples suggests that a combination of diffusioncontrolled and pseudo-capacitive mechanisms governs Na⁺ storage. Additionally, the capacitive and diffusion contributions were quantified at each scan rate for all samples (Figures S19b-h, Supporting Information, middle column, and \$19c-i, Supporting Information, last column, Note S4, Supporting Information). Notably, NFM'PM00 (Figure 6b,c) exhibits a lower diffusion contribution compared to NFM'PM20 (Figure 6e,f). The higher diffusion contribution in NFM'PM20 is typically associated with intercalation-based Na+ storage, which enhances structural stability and enables superior capacity retention over prolonged cycling.

The diffusion coefficients of Na+ (calculated using the Randles-Sevcik equation, see Note \$5 and Table \$6, Supporting Information) were used to elucidate charge transport across the electrodes. A linear curve can be observed when i_p is plotted against $v^{1/2}$, whose slope defines the Na⁺ diffusion (Figure S18f, Supporting Information). From Figure 6g, NFM'PM20 outperforms all others in terms of charge transport with a diffusion coefficient value of 2.54 \times 10⁻¹¹ cm⁻² s⁻¹ (anodic) and 3.36 \times 10⁻¹¹ cm⁻² s⁻¹ (cathodic). In contrast, NFM'PM00 exhibits the lowest diffusion coefficient (1.47 \times 10⁻¹¹ cm⁻² s⁻¹ for anodic, 2.02 \times 10⁻¹¹ cm⁻² s⁻¹ for cathodic) among all the samples, which further reiterates our observations of enhanced electrochemical performance post-doping. Additionally, the overlapping CV curves (for the initial 5 cycles) in all the electrodes at a scan rate of 0.15 mV s⁻¹ indicate the highly reversible storage of Na⁺ (Figure S20a-m, Supporting Information, first column). Voltage stability during cycling is a crucial parameter that can directly impact irreversible capacity losses. Voltage decays were measured from the GCD curves (at 0.2 C) for each cycle up to 350 cycles (Figure 6h). NFM'PM00 exhibits a severe voltage decay, which is suppressed

to some extent in the optimized samples (NFM'PM20). More specifically, the voltage drop for NFM'PM20 after 350 cycles was 1.14 mV per cycle, which is comparatively lower than that of NFM'PM00 (1.40 mV per cycle). Further analysis of voltage decay over 250 GCD cycles at a 0.1C rate (Figure S18g–k, Supporting Information) revealed that the doped samples NFM'PM10, NFM'PM20, NFM'PM30, and NFM'PM40 experienced voltage drops of 462.4, 391.8, 343.4, and 280.3 mV, respectively, all of which were lower than the 469.0 mV recorded for NFM'PM00. In NFM'PM20, the voltage polarization and voltage decay were suppressed, leading to excellent energy conversion efficiency and charge storage capability as compared to NFM'PM00. [31]

Additionally, to investigate Na⁺ dynamics in cathode materials, the GITT was employed. The GITT profiles of all cathodes during the charge/discharge process are shown in Figure 6i. The single titration step for NFM'PM20 during the charging process and the relation between the voltage (V) versus the square root of time $(\tau^{1/2})$ are shown in Figure 6l and Figure S21a-i (Supporting Information), respectively. The evaluated Na⁺ diffusion coefficient (using Fick's second law of diffusion, Note S6, Supporting Information) is shown in Figure 6j (charging) and Figure 6k (discharging). It can be seen that NFM'PM20 displays a higher average Na⁺ diffusion coefficient in both the charge and discharge processes compared to others. For example, NFM'PM20 exhibits the average charge diffusion coefficient of 3.99×10^{-10} cm² s⁻¹, and a discharge diffusion coefficient of 1.51×10^{-9} cm² s⁻¹. In contrast, NFM'PM00 shows a lower average diffusion coefficient $(2.91 \times 10^{-10} \text{ cm}^2 \text{ s}^{-1} \text{ during charge, and } 6.24 \times 10^{-10} \text{ cm}^2 \text{ s}^{-1} \text{ dur-}$ ing discharge). Furthermore, it is noteworthy that lower diffusion coefficients are observed for all cathodes in the voltage range of 2.4 to 2.7 V. These observations align with the charge/discharge profiles, where the maximum capacity is achieved within the voltage plateau between 2.4 and 2.7 V. The diffusion behavior in this region can be attributed to the delayed Na+ (de)insertion process, which typically occurs when the electrode material experiences slower ion migration due to structural changes. Additionally, the XRD of NFM'PM cathodes revealed a lattice expansion post-doping, which also contributes to enhanced Na+ diffusion kinetics during the (de)insertion process.

To examine the effect of the multi-ion dopant on the overall redox kinetics of the NFM'PM cathodes, electrochemical impedance spectroscopy (EIS) was employed. The Nyquist plot was recorded for all samples at open circuit voltage (OCV) are shown in Figure 7a. A semicircle in the high-to-mid-frequency range represents charge transfer resistance (R_{ct}) at the electrodeelectrolyte interface. In contrast, a spike in the low-frequency region corresponds to semi-infinite Warburg diffusion impedance (W) in the bulk. The fitted Nyquist plots using the equivalent circuit (shown in Figure S20a-e, Supporting Information) show the R_{ct} values of NFM'PM00, NFM'PM10, NFM'PM20, NFM'PM30, and NFM'PM40 as 220.57, 194.79, 130.04, 173.28, and 162.41 Ω , respectively (Figure 7b; and Table S7, Supporting Information). Moreover, temperature-dependent EIS analyses were carried out to probe the apparent activation energy (E_a) of Na+ during (de)insertion into NFM'PM00 and NFM'PM20 cathodes (Figure 7c,d). Using the Arrhenius equation (Note S8, Supporting Information), the plot of $log(R_{ct}^{-1}, \Omega)$ versus 1000/T (K⁻¹) is displayed in Figure 7e. The results of linear fitting in Figure 7e illustrate that NFM'PM20 exhibits lower E_a

16163028, 0, Downloaded from https://advanced.onlinelibrary.wiley.com/doi/10.1002/adfm.202517539 by Raghavan Ra

Indian Institute of Technology Gandhinagar, Wiley Online Library on [23/09/2025]. See the Term

on Wiley Online Library for rules of use; OA articles are governed by the applicable Creative

www.afm-journal.de

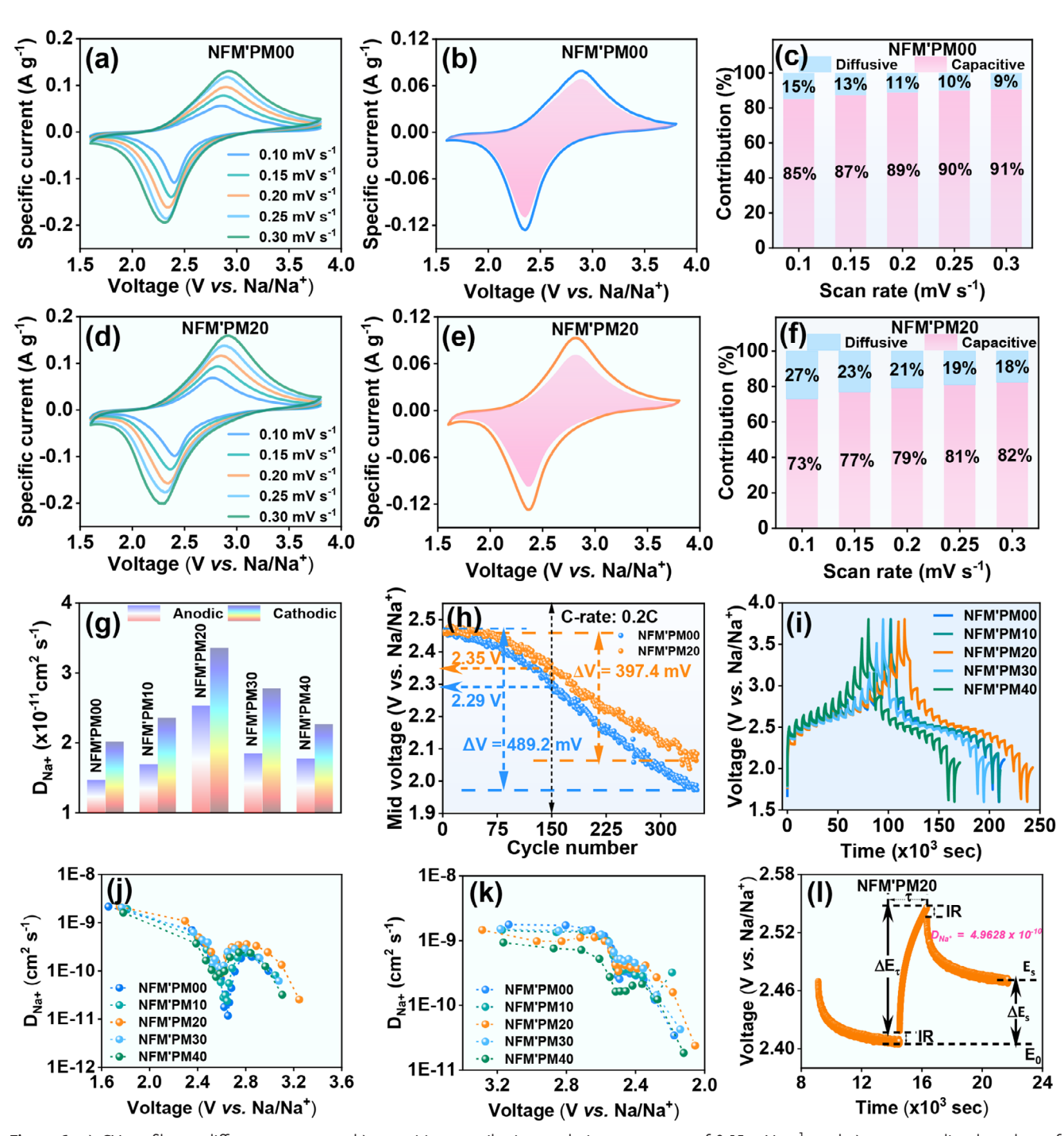


Figure 6. a) CV profiles at different scan rates, b) capacitive contribution analysis at scan rate of 0.15 mV s⁻¹, and c) corresponding bar plots of MFM'PM00; Similarly, d) CV profiles at different scan rates, e) capacitive contribution analysis (at 0.15 mV s⁻¹), and f) bar plots of NFM'PM20; g) Na⁺ diffusion co-efficient using CV test; h) Voltage drop comparison of NFM'PM00 and NFM'PM20 over 350 cycles; i) GITT profiles, j) Charge, and k) Discharge diffusion co-efficient for all samples; l) Single titration step for NFM'PM20 sample at 2.5 V versus Na/Na⁺.

values (15.63 KJ $\rm mol^{-1}$) compared to NFM'PM00 (17.59 KJ $\rm mol^{-1}$, Figure 7f). Overall, the lower R_{ct} values and Na⁺ activation energy of NFM'PM20 compared to NFM'PM00 indicate enhanced charge transfer efficiency, accelerated Na⁺ kinetics, and reduced interfacial resistance, resulting in improved electrochemical performance.

To gain deeper insights into the electrochemical reaction kinetics and to differentiate between them, in-situ EIS and DRT analyses were conducted on the NFM'PM00 and NFM'PM20 cathodes. The EIS spectra recorded during the second cycle for NFM'PM00 and NFM'PM20 are presented in Figure 7g,j, respectively. As the charging and discharging progress, the semicircle in the Nyquist

16163028, 0, Downloaded from https://advanced.onlinelibrary.wiley.com/doi/10.1002/adfm.202517539 by Raghavan Ranganathan - Indian Institute of Technology Gandhinagar , Wiley Online Library on [23.09/2025]. See the Terms

und-conditions) on Wiley Online Library for rules of use; OA articles are governed by the applicable Creative Commons License

www.afm-journal.de

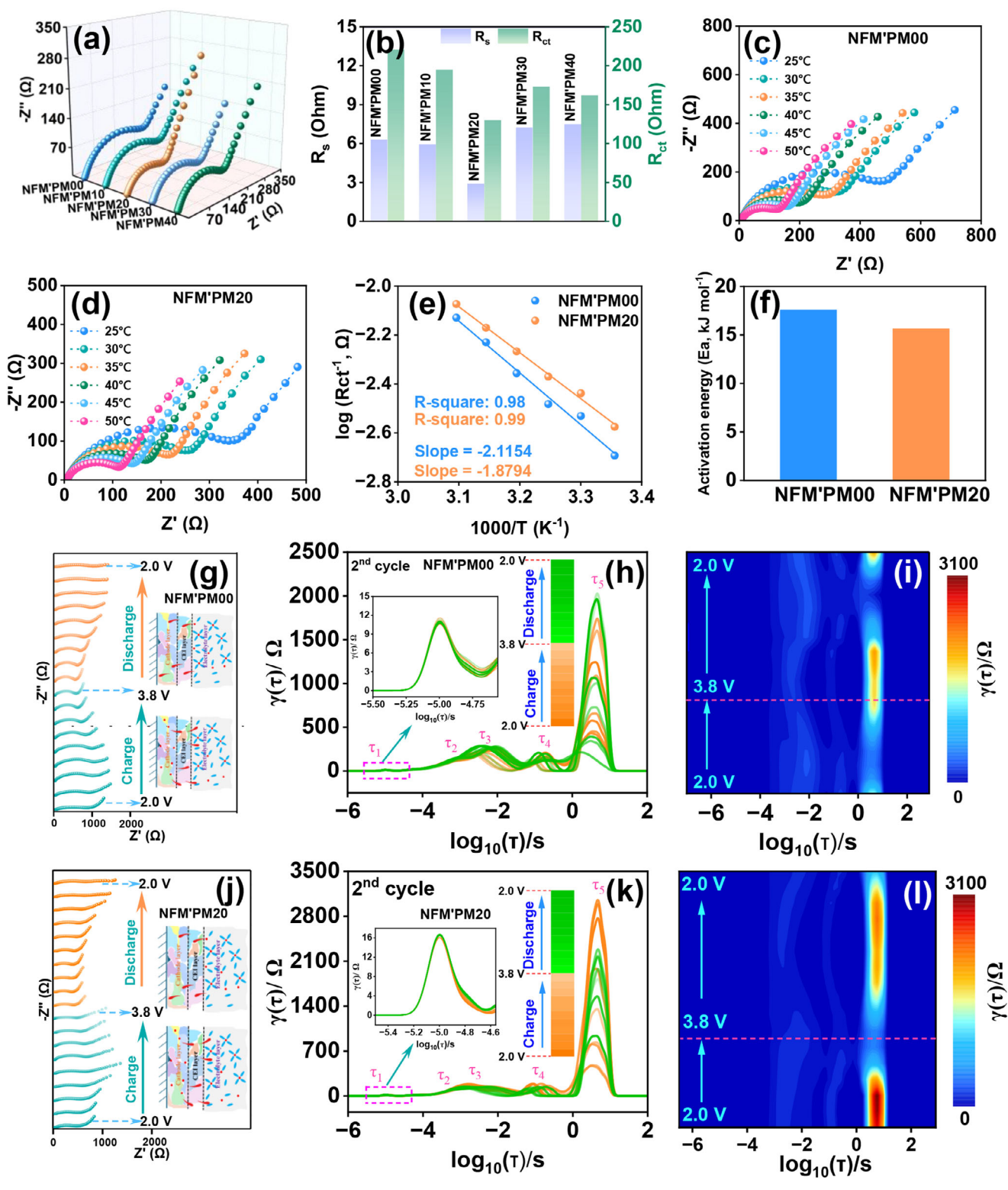


Figure 7. a) Nyquist plots and corresponding, b) Charge transfer and solution resistance for all samples; Temperature-dependent Nyquist plots for c) NFM'PM00, and d) NFM'PM20; e) The relation between the log (Rct⁻¹) versus (1/T), and f) Activation energy for NFM'PM00 and NFM'PM20; g) The in situ EIS plots and corresponding h) DRT profiles and i) 2D contour plot for NFM'PM00; similarly j) The in situ EIS plots and corresponding, k) DRT profiles, and l) 2D contour plot for NFM'PM20.





www.afm-journal.de

plot initially contracts and then expands. In the equivalent circuit (Figure S22g, Supporting Information), incorporating a new cathode electrolyte interphase (i.e., R_{CEI} in series with Warburg) provides a better fit compared to the equivalent circuit without this interface (Figure S22f, Tables S8 and S9, Supporting Information). It is important to note that the distinct trends of EIS profiles are observed in the pristine and modified cathodes (particularly at a charge of 3.8 V). This feature can be ascribed to changes in the R_{ct} and R_{CEI}. The CEI plays a crucial role in modifying the surface chemistry of the electrode, which directly influences interfacial stability, ion transport, and overall charge-storage behavior. The NFM'PM00 displays a pronounced increase in R_{ct} (226.19 $\Omega)$ and R_{CEI} (261.14 $\Omega)$ at 3.8 V, reflecting the formation of a less stable and resistive CEI layer along with sluggish Na⁺ diffusion kinetics at high potentials. In contrast, the modified NFM'PM20 exhibits a much smaller rise in both R_{ct} (167.03 Ω) and R_{CEI} (172.14 Ω), which indicates that the entropy engineering strategy facilitates the formation of a more uniform and stable CEI and maintains efficient Na⁺ transport even at elevated voltages. Also, the detailed analysis of resistance components and diffusion coefficients is discussed below. Moreover, DRT analysis was employed to understand the electrochemical kinetics during battery operation. In Figure 7h (NFM'PM00) and Figure 7k (NFM'PM20), five distinct peaks labeled as τ_1 , τ_2 , τ_3 , τ_4 , and τ_5 cab be observed. The corresponding variations in peak shapes are illustrated in the 2D contour plots in Figure 7i (NFM'PM00) and Figure 71 (NFM'PM20). The position of peaks obtained through the DRT technique represents the different electrochemical processes. Based on the time constant (τ) values, these processes can be classified into four distinct electrochemical mechanisms. Specifically, $\tau \le 10^{-3}$ s corresponds to collector contact resistance, while values between 10⁻³ and 10⁻² s indicate charge transfer resistance. Meanwhile, τ values ranging from 10^{-2} to 10^{-1} s represent charge transport resistance within the cathode and electrolyte, whereas $\tau \ge 10^{-1}$ s reflects the bulk resistance associated with Na⁺ diffusion. The τ_1 peaks at \approx 6.7 ms (NFM'PM00) and ≈6.8 ms (NFM'PM20) signify the charge transfer resistance. This process can be further categorized into two steps: charge transfer within the structure and charge transfer between the material and the CEI/carbon layer. The doped sample exhibits a lower R_{ct} due to the metallic nature of Mn²⁺ and Cr^{3+,} as well as the presence of electron-deficient Al3+ from In3+. The lower R_{ct} in NFM'PM20 is attributed to multi-ion dopants, which effectively reduce R_{ct} within and between the crystal structure. Meanwhile, electron-deficient sites act as electron acceptors, further lowering resistance at the crystal lattice/CEI interface and the carbon layer, thereby enhancing charge transfer efficiency. The three peaks, τ_2 , τ_3 , and τ_4 , lie in the range of 44.6 to 60 ms, primarily associated with Na+ transport at the electrode-electrolyte interface. The τ_5 peaks, observed at 1.92 s for NFM'PM00 and 2.03 s for NFM'PM20, exhibit the highest peak intensity, indicating that electrode bulk diffusion is the primary rate-limiting step. Thus, in-situ EIS and DRT analysis reveal that the entropyengineering strategy enhances interfacial charge transfer, CEI stability, and Na+ transport across NFM'PM20. However, the electrode bulk diffusion remains the primary rate-limiting step, influencing overall battery performance.

To quantitatively assess the characteristics of the CEI layer, the evolution of impedance was systematically probed throughout

the charge/discharge cycles. For MFM'PM00, the R_{CEI} values vary from 248.46 to 432.37 Ω (over the complete cycle) with an average value of 349.25 Ω (Figure 8a). In contrast, for NFM'PM20, the resistance varies from 45.39 to 215.33 Ω with an average value of 134.27 Ω (Figure 8b). The significantly lower R_{CFI} in the optimized sample indicates the formation of a thinner CEI layer compared to the pristine electrode, effectively enhancing ion transport across the electrode surface. Also, the higher R_{et} value in NFM'PM00 compared to NFM'PM20 aligns with our EIS results observed at OCV. In contrast, the average Warburg impedance obtained from in situ EIS analysis is slightly higher for NFM'PM20 (412.38 Ω s^{-1/2}) compared to NFM'PM00 (400.51 Ω s^{-1/2}). This modest increase does not significantly hinder the overall Na⁺ transport kinetics or electrochemical performance, as evidenced by the superior rate capability and cycling stability of NFM'PM20. Also, to understand the improved Na+ conductivity in both samples, the Na^+ diffusion coefficient (D_{Na+}) was calculated using EIS (see Figure 8a,b; and Note S7, Supporting Information). Here, D_{Na+} and σ (representing the Warburg coefficient) exhibit a negative correlation. σ is determined using the slope of the linearly fitted Z' versus $\omega^{-1/2}$ (in the lower frequency region) for each EIS spectrum (Figure \$23, Supporting Information). In all, from EIS, the reduced R_{ct}, R_{CEI}, and increased Na⁺ diffusion for NFM'PM20 reiterate the positive role of multi-ion dopants at the redox-active sites of the cathode.

2.4. In-Situ and Postmortem Analysis of Battery

To depict the charge storage mechanism and structural evolution of NFM'PM20 during Na⁺ insertion/extraction, in-situ XRD analysis was performed. The 2D contour map and in-situ XRD patterns along with the charge/discharge cycles are shown in Figure 8c,d, respectively. The prominent diffraction peaks observed at (112), (022), (32-1), and (420) confirm the formation of a monoclinic phase (s.g. P 2/c) despite the electrode processing.

During the discharge process, all diffraction peaks shifted toward lower angles, signifying the expansion of the lattice framework due to Na⁺ insertion. Notably, upon charging, all peaks progressively return closely to their original Bragg positions, highlighting the remarkable structural stability and reversibility of the material. Furthermore, no occurrence of new diffraction peaks and the retention of existing ones throughout the cycle confirm that NFM'PM20 exhibits a solid solution single-phase Na⁺ storage mechanism. Notably, the (420) diffraction peak exhibits a more pronounced angular shift ($\Delta\theta=1.05^{\circ}$) compared to other peaks, indicating an expansion of the octahedral (Fe/MO₆) units. Such localized rearrangement and expansion of the octahedra can be observed due to the continuous extraction of Na⁺ ions, leading to the intensified electrostatic interactions between the surrounding Fe³⁺ cations. [³³]

Further, the structural parameters of NFM'PM20 are obtained by performing Rietveld refinement of in-situ XRD patterns (for the first charge/discharge cycle). The refined in-situ XRD patterns at the selective (de)sodiation sites (1st, 10th,15th,20th, 30th, and 40th) in the first cycle are shown in Figure S31 (Supporting Information). During the discharging, the lattice parameters (a, b, c) are gradually increased and successfully recovered reversibly with minimal change $(\Delta a/a = 2.47\%, \Delta b/b = 2.65\%,$

www.afm-journal.de

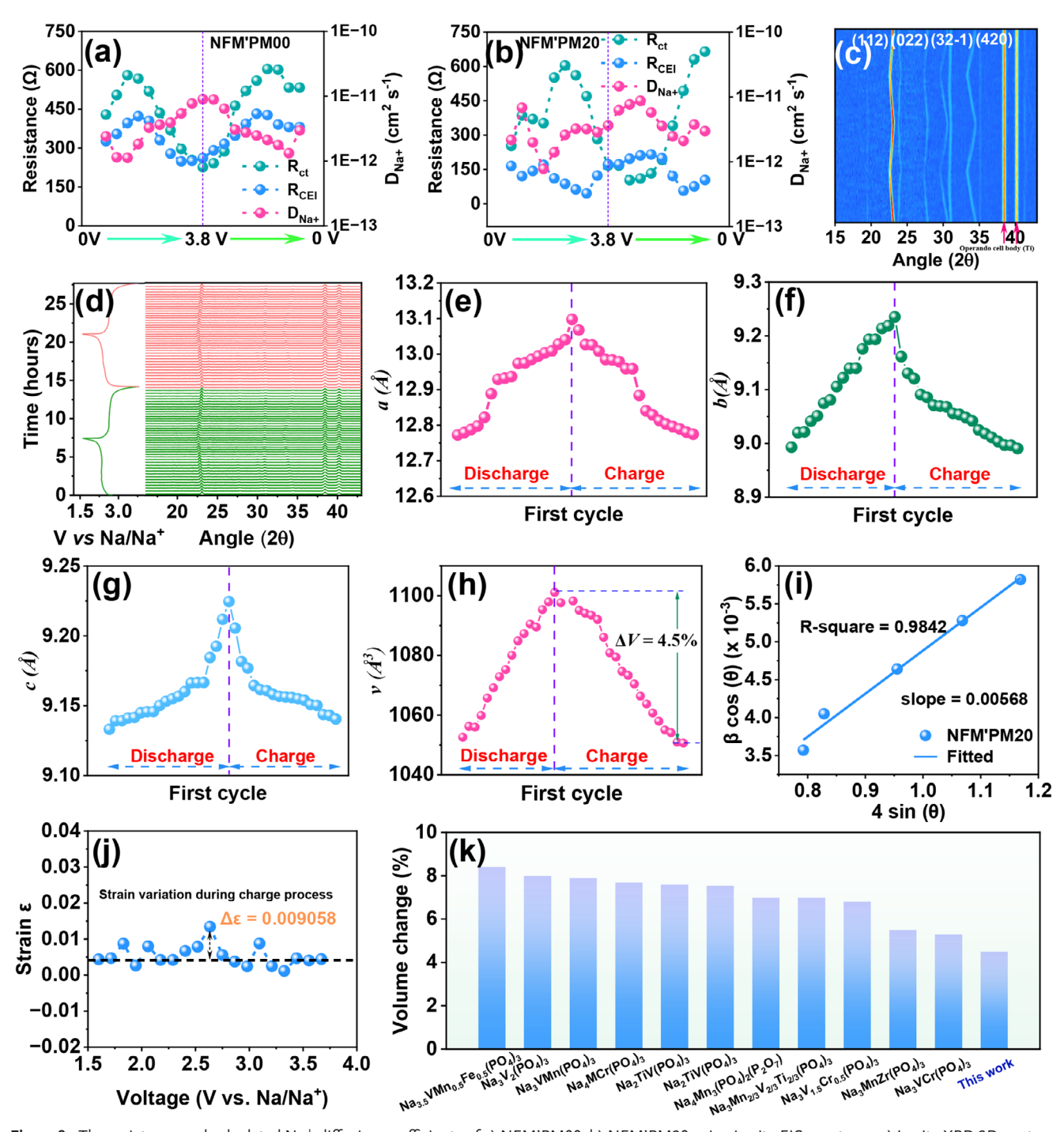


Figure 8. The resistance and calculated Na⁺ diffusion coefficients of a) NFM'PM00, b) NFM'PM20 using in situ EIS spectrum; c) In situ XRD 2D contour plot, and d) Charge/discharge profiles along with XRD patterns of NFM'PM20; e–g) The variation of lattice parameters during 1st charge/discharge cycle, and h) Corresponding volume change of NFM'PM20; i) The linear behavior of Willaim-son-Hall plot and, j) lattice strain evaluation in NFM'PM20; k) Comparison of volume variation of prepared material with some reported cathode materials for NIBs.

 $\Delta c/c = 0.91\%$) during subsequent charging (Figure 8e–g). Moreover, the successive decrease in the c parameter during charging is beneficial for shortening the Na⁺ diffusion pathways. Despite the localized rearrangement and expansion of Fe/MO₆, NFM'PM20 exhibits a volume change of only 4.5% (Figure 8h), which is significantly lower than most of the reported NASICON

cathodes, such as Na $_3$ V $_2$ (PO $_4$) $_3$ (8.0%), Na $_3$ VMn(PO $_4$) $_3$ (7.9%), Na $_4$ VMn(PO $_4$) $_3$ (7.7%), Na $_2$ TiV(PO $_4$) $_3$ (7.6%), Na $_2$ TiV(PO $_4$) $_3$ (7.55%), Na $_4$ Mn $_3$ (PO $_4$) $_2$ (P $_2$ O $_7$) (7.0%), Na $_3$ Mn $_2$ (PO $_4$) $_3$ (6.8%), Na $_3$ MnZr(PO $_4$) $_3$ (5.50%), Na $_3$ VCr(PO $_4$) $_3$ (5.3%) (Figure 8k). (4a,21,34) Additionally, using these in-situ XRD patterns, the strain variation in the lattice





www.afm-journal.de

dimensions was analyzed using the Williamson-Hall method (Figure 8i; and Note S9, Supporting Information).[31] The experimental data from the selected Williamson-Hall plots validate the high accuracy of lattice strain estimation. As shown in Figure 8j, the lattice strain of NFM'PM20 progressively increases with charge depth, reaching its peak value of 0.00906 at 2.6 V. This strain evolution closely correlates with the chargedischarge profiles, as the structure undergoes the highest strain within the voltage range of 2.4-2.7 V. This phenomenon is attributed to the intensified Na⁺ interactions, which coincide with the maximum charge storage capacity. Thus, the minimum volume change and strain variation in NFM'PM20 emphasize the critical role of entropy-engineering strategy in NFPM cathodes, contributing to enhanced Na⁺ storage performance.

To illustrate the changes in the valence state of the redoxactive centers and sodium-ion interaction with dopants, ex-situ XPS of NFM'PM00 and NFM'PM20 were carried out at various charge (1.6, 3.0, and 3.8 V) and discharge states (3.5, 2.5, and 2.2 V). The analysis of Fe 2p spectra revealed variations corresponding to charge/discharge cycles (Figure 9a,b). Upon full discharge (1.6 V) of the battery from its OCV, two distinct oxidation states of Fe (Fe²⁺ and Fe³⁺) were detected. This can be attributed to the incomplete electrochemical conversion of Fe resulting from discharge initiated at the OCV. During subsequent charging to 3.0 V, a reduction in the peak intensity of Fe²⁺ was observed, along with a significant increase in the peak intensity of Fe³⁺, indicating the oxidation of Fe²⁺ to Fe³⁺. As charging progressed to 3.8 V (100% state of charge, SOC), only Fe3+ peaks were detected, signifying the complete oxidation of Fe²⁺. During the subsequent discharge from 3.8 to 2.2 V, Fe³⁺ underwent a gradual reduction to Fe2+, demonstrating the highly reversible redox activity of iron. For the dopant elements Cr 2p, In 3d, Mn 2p, Zn 2p, and Al 2p, their binding energies remain unchanged over the entire charge/discharge cycle (Figure S24, Supporting Information). These results confirm their role as electrochemically inactive stabilizers, which can enhance the structural integrity of the electrode material, improve cycling stability, and mitigate capacity degradation over prolonged operation. Furthermore, the core elements, including Na 1s, Mo 3d, and P 2p, that were deconvoluted for both samples, reveal no significant variations during (de)sodiation when compared to the pristine electrode (Figures S24 and S25, Supporting Information). However, the identification of organic species proved challenging due to the presence of a polyvinylidene difluoride (PVDF) binder and conductive additives, which prevented the deconvolution of the C 1s and O 1s spectra. Overall, ex-situ XPS analysis confirms that the Fe²⁺/Fe³⁺ redox process serves as the principal charge compensation mechanism (as illustrated in Figure S26, Supporting Information) in NFM'PM00 and NFM'PM20 cathodes. To understand the structural stability after deep cycling at 2 C, ex-situ XRD patterns of electrodes was recorded for NFM'PM20 (Figure 9c) and NFM'PM00 (Figure \$27, Supporting Information) at the 25th, 50th, 75th, 100th, 150th, and 200th cycles. The XRD exhibits peaks similar to those of pristine electrodes, indicating the material's ability to maintain its original phase throughout charge/discharge cycling. Furthermore, the minimal variation in diffraction peak intensities over repeated cycling suggests the material retains a highly ordered crystalline structure, demonstrating its structural

stability and phase integrity during prolonged electrochemical operation.

As highlighted in the previous sections, the advantage of utilizing the multi-ion dopants stems from their cumulative effect, wherein the dopants contribute to a cocktail effect, significantly enhancing charge storage performance. Given the critical role of electrode/electrolyte interfaces, their influence on the cycling stability and rate capability of electrode materials is profound. Moreover, the kinetics of Na+ transport are significantly modulated by the interphase structure and the bulk electrode composition. A thin and uniform CEI can effectively isolate the direct contact between the electrode and electrolyte, thereby impeding the oxidation/reduction of the electrolyte. Conversely, thick and uneven CEI results in excessive electrolyte consumption, leading to diminished Na+ conductivity and inhibiting rapid and reversible Na+ diffusion across the interface. Therefore, investigation of CEI formation is crucial for optimizing electrode performance. In this regard, ex-situ TEM imaging conducted after the first charge/discharge cycle was employed to assess the thickness and uniformity of the CEI layer. The TEM analysis revealed that NFM'PM00 exhibits uneven and thick CEI ranging from 12-15 nm (Figure 9d). In contrast, the NFM'PM20 is completely covered with a nearly uniform CEI of ≈5 nm thick (Figure 9e). The reduced CEI thickness in NFM'PM20 compared to NFM'PM00 significantly facilitates Na+ transport by effectively lowering the charge transfer impedance. The schematic diagram of CEI formation on NFM'PM20 is shown in Figure 9f. These findings are further corroborated by in-situ EIS measurements, which indicate a higher charge transfer resistance (R_{ct}) for NFM'PM00 than for NFM'PM20. Additionally, a pronounced increase in semicircle diameter after the first cycle was observed in in-situ EIS (Figure 7g,j) compared to normal EIS recorded at an OCV (Figure 7a). This increase further confirms the formation of the CEI layer on both cathode materials. The formation of such a protective layer offers several advantages: it reduces electrolyteinduced corrosion on the electrode surface, suppresses undesirable secondary reactions, and effectively inhibits the dissolution of the cathode material.[13] Consequently, it helps preserve the structural integrity of the electrode by maintaining a phase purity, high crystallinity, and stability over extended cycling periods.

To gain deeper insights into these structural properties, TEM analysis was conducted on NFM'PM00 and NFM'PM20 electrodes after 300 charge/discharge cycles. The TEM images of NFM'PM00 (Figure S28, Supporting Information) and NFM'PM20 (Figure S29, Supporting Information) confirm that both materials retain their crystallinity. Furthermore, the presence of well-defined lattice fringes (Figure 9h,k) and sharp diffraction spots in the SAED patterns (insets of Figure 9g,j) further validates their highly crystalline nature. Additionally, the measured lattice spacing for NFM'PM00 (Figure 9h,i) and NFM'PM20 (Figure 9k,l) was ≈ 0.8232 and 0.7622 nm, respectively. Notably, the minimal increase in lattice spacing of 6.19% in NFM'PM20 (relative to the pristine state, Figure 40) compared to a 23.53% increase in NFM'PM00 (relative to the pristine state, Figure 4g) highlights the enhanced structural stability of the optimized sample, demonstrating the effectiveness of the entropyengineering strategy in improving electrode durability. The insitu XRD analysis (discussed above) of NFM'PM20 also revealed minimal volume changes, which aligns well with these results.

Adv. Funct. Mater. 2025, e17539

16163028, 0, Downloaded from https://advanced.onlinelibrary.wiley.com/doi/10.1002/adfm.202517539 by Raghavan Ranganathan

Indian Institute of Technology Gandhinagar, Wiley Online Library on [23/09/2025]. See the Terms

on Wiley Online Library for rules of use; OA articles are governed by the applicable Creative Commons License

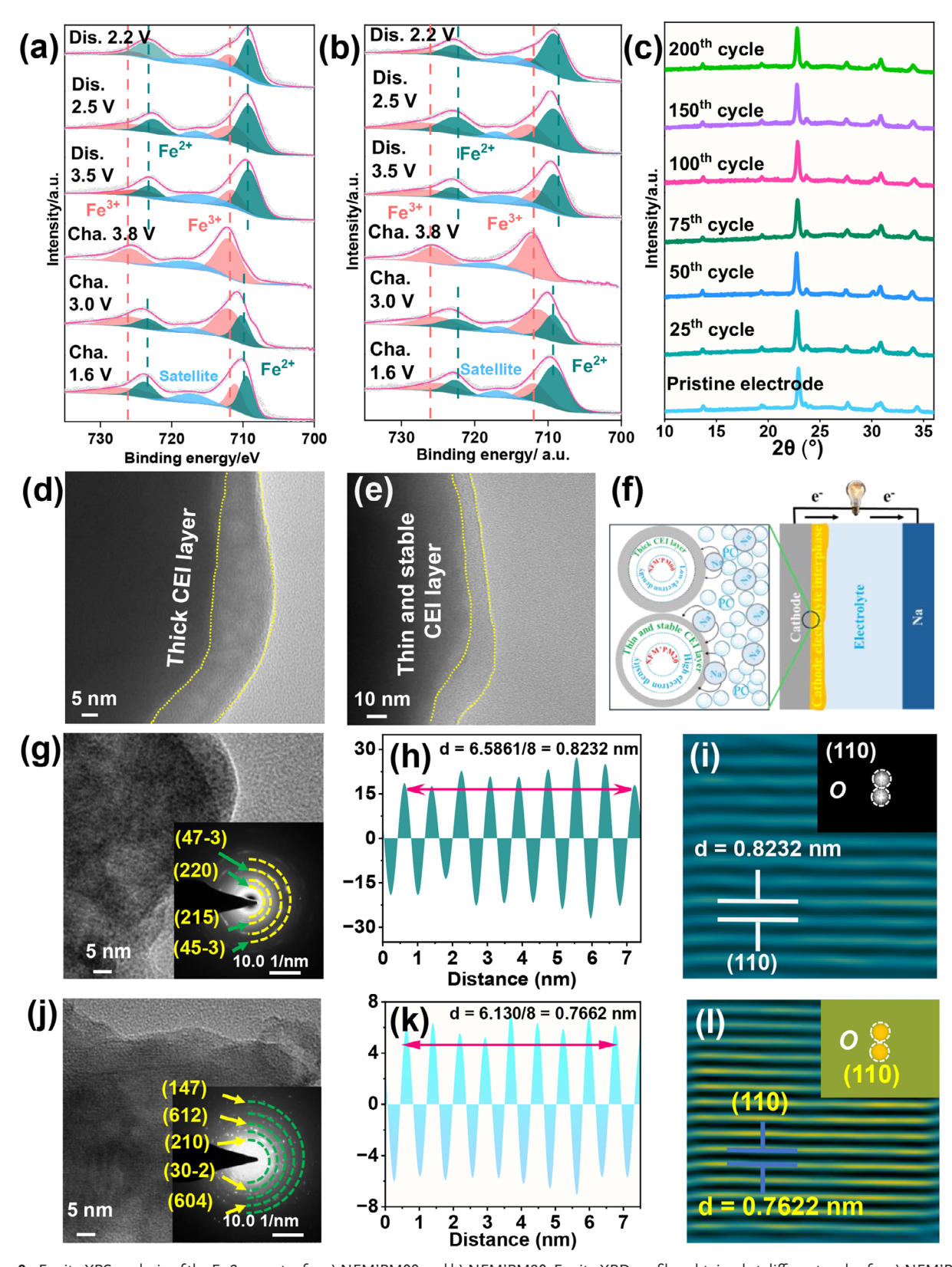


Figure 9. Ex situ XPS analysis of the Fe 2p spectra for a) NFM'PM00 and b) NFM'PM20; Ex situ XRD profiles obtained at different cycles for c) NFM'PM20; CEI layer analysis using TEM images for d) NFM'PM00 and e) NFM'PM20; f) Schematic representation of the CEI layer formation on NFM'PM20 cathode; g) Evolution of lattice fringes and SAED patterns, h) d-spacing, and i) FFT analysis in NFM'PM00; Similarly, j) lattice fringes and SAED patterns, k) d-spacing, and l) FFT analysis in NFM'PM20 after 300 cycles.





www.afm-journal.de

To understand the electrode microstructure, ex-situ SEM analysis was conducted on both samples in their pristine states and after 400 charge/discharge cycles. The pristine uncycled electrodes are flat, and the particles are uniformly distributed on the surface and cross sectional area of the electrodes (Figure \$30a,b, Supporting Information). After 400 cycles at 2C, the NFM'PM20 electrode remains structurally intact, with no visible cracks observed (Figure S30d, Supporting Information). In contrast, noticeable crack formation is evident in the NFM'PM00 electrode (Figure \$30c, Supporting Information). The progressive accumulation of internal stress during prolonged cycling can induce mechanical degradation of the material, potentially leading to particle fracture, structural rearrangement, localized density variations, and the formation of cracks.^[35] Subsequently, this can result in significant capacity fading, leading to the marginal electrochemical performance of the NFM'PM00 cathode.

2.5. DFT Studies, Na⁺ Migration, and Electron Dynamics

Experimental results explicitly confirm that the strategic modulation of multi-ion dopants significantly enhances the electrical conductivity, ion transport kinetics, and structural stability of the material. To obtain a deeper insight into these fundamental properties, DFT calculations for the undoped NFM'PM00 and doped NFM'PM20 cathodes were performed using the Vienna Ab-initio simulation package (VASP).[36] The Perdew-Burke-Ernzerhof (PBE) generalized gradient approximation exchange-correlation functional was used in all calculations.[37] Spin-polarized calculations were employed due to the presence of elements like Fe and Mo. The energy and force tolerances in the case of NFM'PM00 were 10^{-6} and 2×10^{-2} , respectively. A dense Kpoint Monkhorst-Pack mesh with $12 \times 12 \times 12$ points was used in the k-space. [38] Dudarev DFT+U Hubbard parameters were used for d-block elements.[39] The optimized theoretical crystal structures of NFM'PM00 and NFM'PM20 are shown in Figure 10a,b, respectively. The bond valence sum (BVS) method, [40] was effectively employed using softBV software, [41] to map localized Na+ transport pathways and substantiate ion migration mechanisms, offering valuable insights into diffusion behavior in both samples (Figure 10c,d). The well-organized, inter-bridged, and widened transport channels in NFM'PM20 ensure faster Na⁺ diffusion in the lattice framework. Using these diffusion pathways, the Na+ Bond Valence Sum Energy (BVSE) landscape is shown in Figure 10e. Notably, NFM'PM20 exhibits a lower energy barrier (0.45 eV) compared to the NFM'PM00 (0.6 eV). These results illustrate that NFM'PM20 enables facile Na+ diffusion kinetics with deeper Na⁺ insertion/de-insertion, as corroborated by the diffusion coefficient obtained from the CV, GITT, and EIS tests. Such a reduced energy barrier and enhanced diffusion process achieved through entropy regulation led to an accelerated electrode redox kinetics. Furthermore, to better understand the effectiveness of entropy engineering on the electrical properties of the material, the density of states (DOS) and electronic structures were obtained from the relaxed crystal structure at highsymmetry K points.

The spin-polarized contributions from Fe atoms are illustrated in red color for both spin-up and spin-down states (Figure 10f). In NFM'PM00, the Fermi energy (E_{F}) level is near the conduction

band. Both Mo and Fe bands are closer to E_F and play a vital role. The calculated energy bandgap (Eg) of NFM'PM00 is 1.926 eV (Figure 10g). It is important to note that DFT-GGA can underpredict bandgaps by 30-40%. [42] While this is significant for widebandgap semiconductors (Eg > 5 eV), this is not significant in our case, as the error is $\approx 0.58-0.77$ eV. For the MFM'PM20 sample, the sqsgenerator software was used to substitute Fe atoms with Mn, Cr, Al, In, and Zn in equi-proportion.^[43] The Special Quasirandom Structures (SQS) technique ensures that the substitution results in a thermodynamically stable structure.^[44] The complete DOS and electronic band-structure with only dopant contribution for the doped NFM'PM20 can be seen in Figure 10h,i. While the electronic band structure for the NFM'PM20 is the same as that of NFM'PM00, the E_F level has moved into the valence band due to doping. However, in NFM'PM20, the DOS (Figure 10h) and electronic band structure (Figure 10i) indicate that only the dopants contribute significantly, with the E_E notably shifted into the valence band. The major contributors had been Mn (shown in yellow), Cr (shown in green), and Zn (shown in metallic white). Al and In show negligible (<1%) contribution as the dopant concentrations of 0.04%. According to the calculation, the dopants result in a metallic system with the conduction band moving below the $E_{\scriptscriptstyle F}$ as well.

Additionally, the complementary analyses of the magnetic properties (Table \$10, Supporting Information) and Bader charge distribution (Table \$11, Supporting Information) for NFM'PM00 and NFM'PM20 further substantiate these findings. Magnetic moment analysis shows that while Fe and Mo exhibit slight increases in spin polarization, the introduction of Mn2+ (-3.817 μB) and Cr³⁺ (2.927 μB) contributes pronounced magnetic complexity, indicative of competing magnetic interactions within the NFM'PM20 lattice. These magnetic interactions are likely to influence both electron transport and Na+ diffusion by modulating the local energy landscape. Overall, the entropy-engineering strategy is shown to effectively tailor the bandgap, enhance electronic conductivity, and promote Na+ mobility in NFPM cathodes. Collectively, these structural and electronic modifications lead to significantly improved electrochemical performance, as evidenced by enhanced rate capability, capacity retention, and cycling stability of the designed cathodes. Furthermore, the electrochemical performance achieved in this study is compared with state-of-the-art cathode materials reported for NIB applications, as summarized in Table S12 (Supporting Information).

3. Conclusion

In this work, we have successfully demonstrated the potential of entropy engineering in NASICON-type NaFe₂(PO₄)(MoO₄)₂ cathodes, through strategic multi-cation doping (Mn, Cr, Al, Zn, and In) at Fe sites. We developed an optimized NaFe_{1.8}(MnCrAlZnIn)_{0.2}(PO₄)(MoO₄)₂ (NFM'PM20) cathode that shows 1) exceptional structural stability with minimal volume change (4.5%) and ultralow strain (0.0091) during cycling, 2) enhanced electronic conductivity through bandgap reduction and improved Fe³⁺/Fe²⁺ redox activity, and 3) optimized Na⁺ transport pathways with lowered diffusion barriers. The NFM'PM20 cathode delivers outstanding electrochemical performance, including a high energy density of 315.62 Wh kg⁻¹, remarkable rate capability (82 mAh g⁻¹ at 1C), and

16163028, 0, Downloaded from https://advanced.onlinelibrary.wiley.com/doi/10.1002/adfm.202517539 by Raghavan Ranganathan - Indian Institute of Technology Gandhinagar, Wiley Online Library on [2309/2025]. See the Terms

on Wiley Online Library for rules of use; OA articles are governed by the applicable Creative Commons License

www.afm-journal.de

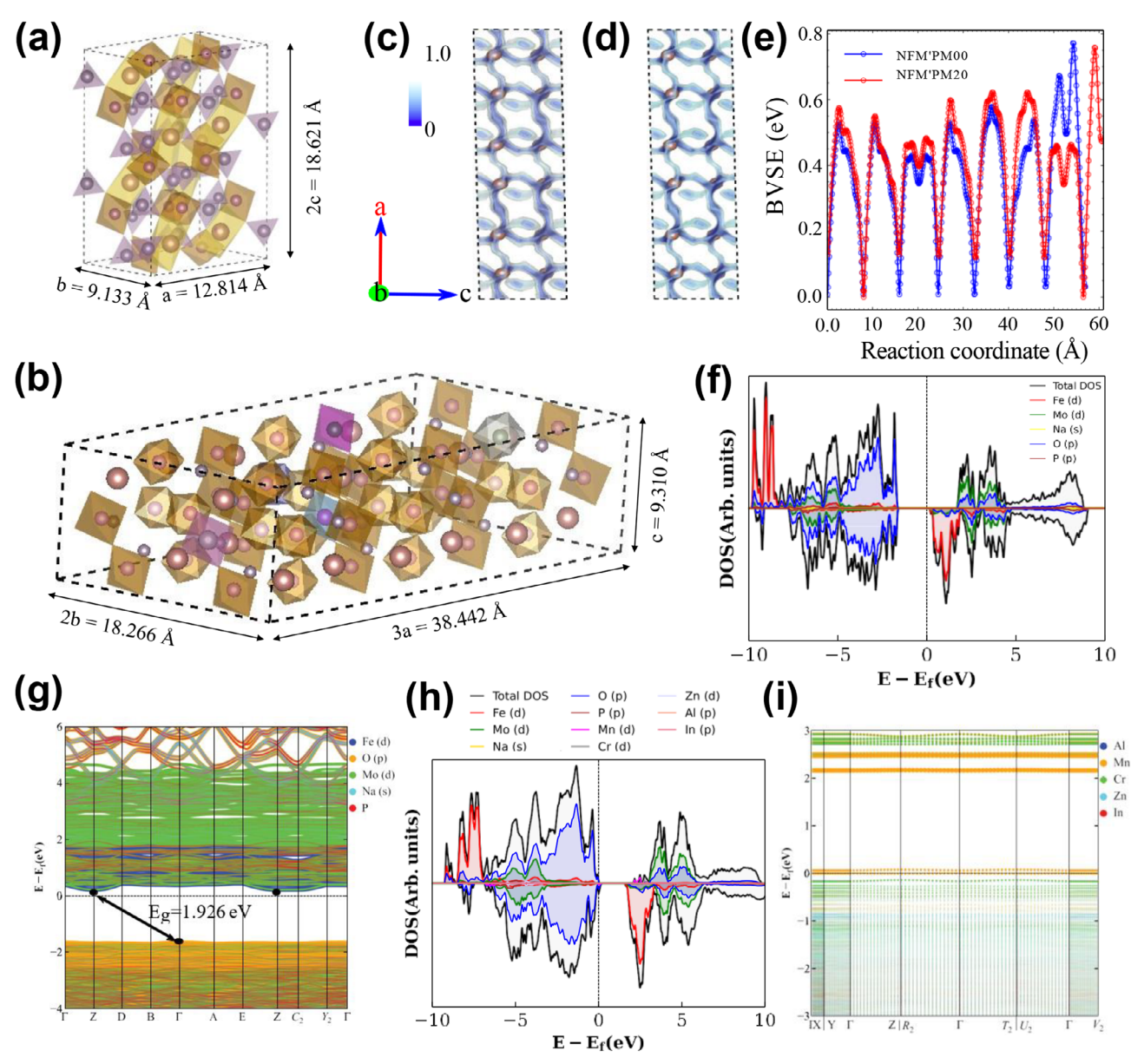


Figure 10. a) Relaxed structure of NFM'PM00 and b) NFM'PM20 obtained from VASP DFT calculation with GGA-PBE functional; c) Na⁺ ion migration pathway for NFM'PM00, d) NFM'PM20; and e) BVSE as a function of reaction coordinate; Electronic DOS of f) NFM'PM00, h) NFM'PM20; and band structure of g) NFM'PM00, i) NFM'PM20.

unprecedented cycling stability (over 2000 cycles at 5C). Through comprehensive characterization, including XRD, EPR, TEM, and DRT analysis, coupled with DFT calculations, we have established clear structure-property relationships that explain these performance enhancements. Notably, our ex-situ TEM, FESEM, XRD, and XPS analyses reveal that the entropy modification promotes the formation of a thinner, more uniform, and stable CEI layer compared to the pristine material. The DRT analysis further confirms reduced charge transfer impedance at the electrode-electrolyte interface, highlighting the beneficial role of the modified CEI in enhancing interfacial kinetics. This work provides the first evidence that entropic modification effects can be successfully extended to such unique NASICON frameworks,

which contain transition metal oxide as the polyanion, opening new possibilities for polyanionic cathode design. These findings represent an advancement in NIBs technology, offering both fundamental insights and practical solutions for developing high-performance, cost-effective energy storage systems. Future work should explore the broader application of this approach to other emerging polyanionic systems and investigate the potential for scaling up for commercial implementation.

Supporting Information

Supporting Information is available from the Wiley Online Library or from the author.

16163028, Q. Downloaded from https://advanced.onlinelibrary.wiley.com/doi/10.1002/adfm.202517539 by Raghavan Ranganathan - Indian Institute of Technology Gandhinagar , Wiley Online Library on [23.09/2025]. See the Terms

on Wiley Online Library for rules of use; OA articles are governed by the applicable Creative Commons



Acknowledgements

S.D.P., V.M., and P.M. contributed equally to this work. S.P. acknowledges IISER-Bhopal for providing a fellowship for his Ph.D. R.R.G. acknowledges the Department of Science and Technology and Anusandhan National Research Foundation (earlier DST-SERB), Government of India, for the Startup-Research Grant (SRG), SRG/2022/001017, and the DST-FIST program, SR/FST/ET-II/2022/1017 (C) for funding the work. The Central Instrumentation Facility of IISER-Bhopal is acknowledged for providing access to material characterization facilities. A.K.N. acknowledges funding from the University of Southern Queensland through a capacity-building grant and the Australian Research Council through the ARC Research Hub in New Safe and Reliable Energy Storage and Conversion Technologies (ARC Safer Energy Hub project IH200100035).

Conflict of Interest

The authors declare no conflict of interest.

Data Availability Statement

The data that support the findings of this study are available from the corresponding author upon reasonable request.

Keywords

cathode-electrolyte interphase, DFT, energy density, NASICON, sodium-

Received: July 12, 2025 Revised: September 9, 2025 Published online:

- [1] W. Zuo, X. Liu, J. Qiu, D. Zhang, Z. Xiao, J. Xie, F. Ren, J. Wang, Y. Li, G. F. Ortiz, Nat. Commun. 2021, 12, 4903.
- [2] Z. Lin, Y. Ying, Z. Xu, G. Chen, X. Gong, Z. Wang, D. Guan, L. Zhao, M. Yang, K. Fan, Energy Environ. Sci. 2025, 18, 334.
- [3] a) A. Yao, S. M. Benson, W. C. Chueh, Nat. Energy 2025, 10, 404; b) S. Wang, J. Bai, P. Wang, Y. Mao, K. Xiao, Y. Liu, S. Qiu, X. Zhu, B. Zhao, Y. Sun, Small 2025, 21, 2500566.
- [4] a) L. Zhu, M. Wang, S. Xiang, D. Sun, Y. Tang, H. Wang, Adv. Energy Mater. 2023, 13, 2302046; b) R. Huang, D. Yan, Q. Zhang, G. Zhang, B. Chen, H. Y. Yang, C. Yu, Y. Bai, Adv. Energy Mater. 2024, 14, 2400595.
- [5] a) C. Liu, Z. Zhang, H. Liao, Y. Jiang, Y. Zheng, Z. Li, Y. Gao, Adv. Funct. Mater. 2025, 35, 2424759; b) N. Jiang, X. Wang, H. Zhou, Y. Wang, S. Sun, C. Yang, Y. Liu, Small 2024, 20, 2308681; c) S. D. Pinjari, P. Mudavath, R. C. Dutta, I. Pal, D. Kundu, S. Parshanaboina, A. K. Singh, A. K. Nanjundan, R. R. Gaddam, Small 2025, 21, 2501004.
- [6] a) B. Ouyang, J. Wang, T. He, C. J. Bartel, H. Huo, Y. Wang, V. Lacivita, H. Kim, G. Ceder, Nat. Commun. 2021, 12, 5752; b) Y. Liu, J. Li, Q. Shen, J. Zhang, P. He, X. Qu, Y. Liu, EScience 2022, 2, 10.
- [7] a) X. Ge, H. Li, J. Li, C. Guan, X. Wang, L. He, S. Li, Y. Lai, Z. Zhang, Small 2023, 19, 2302609; b) S. D. Pinjari, R. C. Dutta, S. Chen, P. Mudavath, X. Huang, J. Bell, S. K. Bhatia, A. K. Nanjundan, R. R. Gaddam, Chem. Eng. J. 2024, 493, 152485.
- [8] X. Ge, L. He, C. Guan, X. Wang, J. Li, Y. Lai, Z. Zhang, ACS Nano 2023, 18. 1714.
- [9] a) S. D. Pinjari, R. C. Dutta, S. Parshanaboina, P. Mudavath, S. Singha, D. Dubal, X. Wang, J. Bell, A. K. Nanjundan, R. R. Gaddam, Chem. Eng. J. 2024, 502, 157979; b) J. Zhang, Y. Liu, X. Zhao, L. He, H. Liu, Y. Song, S. Sun, Q. Li, X. Xing, J. Chen, Adv. Mater. 2020, 32, 1906348.

- [10] a) H. Li, M. Xu, H. Long, J. Zheng, L. Zhang, S. Li, C. Guan, Y. Lai, Z. Zhang, Adv. Sci. 2022, 9, 2202082; b) C. Jin, Y. Wang, X. Zhao, J. Jin, Z. Li, X. Qu, L. Jiao, Y. Liu, Adv. Funct. Mater. 2025, 35, 2422101.
- [11] a) M. T. Ahsan, D. Qiu, Z. Ali, Z. Fang, W. Zhao, T. Shen, Y. Hou, Adv. Energy Mater. 2024, 14, 2302733; b) X. Hu, S. Liang, J. Lin, W. Ren, S. Fu, Z. Cao, T. Zhang, L. Zhang, X. Cao, Adv. Energy Mater. 2025, 15,
- [12] G. Li, Y. Cao, J. Chen, K. Zhang, Y. Liu, X. Zhang, Y. Wang, F. Wang, Y. Xia, Small Methods 2024, 8, 2301745.
- [13] X. Hu, H. Li, Z. Wang, M. Liu, Y. Lu, Y. Zhang, J. Li, K. Ding, H. Liu, Z. F. Ma, Adv. Funct. Mater. 2025, 35, 2412730.
- [14] J. W. Yeh, S. K. Chen, S. J. Lin, J. Y. Gan, T. S. Chin, T. T. Shun, C. H. Tsau, S. Y. Chang, Adv. Eng. Mater. 2004, 6, 299.
- [15] a) Y. Zhang, Y. J. Zhou, J. P. Lin, G. L. Chen, P. K. Liaw, Adv. Eng. Mater. 2008, 10, 534; b) A. Takeuchi, A. Inoue, Mater. Trans. 2005, 46,
- [16] G. Li, L. Zhang, Z. Xu, Y. Liu, K. Zhang, S. Zhao, Y. Cao, Y. Xia, Adv. Funct. Mater. 2025, 35, 2425598.
- [17] P. Hou, M. Gong, M. Dong, Z. Lin, J. Huang, H. Zhang, F. Li, Energy Storage Mater. 2024, 72, 103750.
- [18] Y. Wu, Z. Cao, L. Song, J. Gao, ACS Appl. Mater. Interfaces 2021, 13, 48865
- [19] M. Li, C. Sun, Q. Ni, Z. Sun, Y. Liu, Y. Li, L. Li, H. Jin, Y. Zhao, Adv. Energy Mater. 2023, 13, 2203971.
- [20] N. Ahmad, L. Yu, M. U. Muzaffar, B. Peng, Z. Tao, S. Khan, A. Rahman, J. Liang, Z. Jiang, X. Ma, Adv. Energy Mater. 2025, 15, 2404093.
- [21] C. Sun, Y. Zhao, Q. Ni, Z. Sun, X. Yuan, J. Li, H. Jin, Energy Storage Mater. 2022, 49, 291.
- [22] S. Kadam, R. Kate, U. Chothe, P. Chalwadi, J. Shingare, M. Kulkarni, R. Kalubarme, B. Kale, ACS Appl. Mater. Interfaces 2023, 15,
- [23] a) R. Dedryvère, M. Maccario, L. Croguennec, F. Le Cras, C. Delmas, D. Gonbeau, Chem. Mater. 2008, 20, 7164; b) N. A. Kumar, R. R. Gaddam, M. Suresh, S. R. Varanasi, D. Yang, S. K. Bhatia, X. Zhao, J. Mater. Chem. A 2017, 5, 13204.
- [24] H. Li, Y. Wang, X. Zhao, J. Jin, Q. Shen, J. Li, Y. Liu, X. Qu, L. Jiao, Y. Liu, ACS Energy Lett. 2023, 8, 3666.
- [25] C. Xu, J. Zhao, E. Wang, X. Liu, X. Shen, X. Rong, Q. Zheng, G. Ren, N. Zhang, X. Liu, Adv. Energy Mater. 2021, 11, 2100729.
- [26] M. Amanulla, C. M. Magdalane, G. Ramalingam, R. Sundaram, N. Tamam, H. Somaily, M. Al-Buriahi, Appl. Phys. A 2022, 128, 397.
- [27] a) J. V. Barbosa Moura, A. A. Gomes de Souza, P. de Tarso Cavalcante Freire, C. da Luz Lima, T. M. Brito, F. Oliveira, Int. J. Appl. Ceram. Technol. 2021, 18, 615; b) T. Ravindran, V. Sivasubramanian, A. K. Arora, J. Phys.: Condens. Matter 2004, 17, 277.
- [28] S. Chong, J. Yang, L. Sun, S. Guo, Y. Liu, H. K. Liu, ACS Nano 2020, 14, 9807.
- [29] R. Rajagopalan, B. Chen, Z. Zhang, X. L. Wu, Y. Du, Y. Huang, B. Li, Y. Zong, J. Wang, G. H. Nam, Adv. Mater. 2017, 29, 1605694.
- [30] Y. Wang, Y. Sui, Z. Xiao, W. Fei, M. Deng, X. Zhang, H. Guo, R. Wang, L. Wu, Adv. Funct. Mater. 2025, 35, 2500290.
- [31] F. Li, Y. Lin, J. Liu, J. Chen, X. Wan, L. Zhao, L. Xi, Z. Li, H. Zhang, X. Xu, Energy Environ. Sci. 2025, 18, 124.
- [32] Y. Lu, C.-Z. Zhao, J.-Q. Huang, Q. Zhang, Joule 2022, 6, 1172.
- [33] M. Chen, D. Cortie, Z. Hu, H. Jin, S. Wang, Q. Gu, W. Hua, E. Wang, W. Lai, L. Chen, Adv. Energy Mater. 2018, 8, 1800944.
- a) R. Liu, G. Xu, Q. Li, S. Zheng, G. Zheng, Z. Gong, Y. Li, E. Kruskop, R. Fu, Z. Chen, ACS Appl. Mater. Interfaces 2017, 9, 43632; b) F. Lalère, V. Seznec, M. Courty, J. Chotard, C. Masquelier, J. Mater. Chem. A **2018**, *6*, 6654; c) Y. Zhao, X. Gao, H. Gao, H. Jin, J. B. Goodenough, Adv. Funct. Mater. 2020, 30, 1908680; d) H. Gao, I. D. Seymour, S. Xin, L. Xue, G. Henkelman, J. B. Goodenough, J. Am. Chem. Soc. 2018, 140, 18192; e) F. Chen, V. M. Kovrugin, R. David, O. Mentré, F. Fauth, J. N. Chotard, C. Masquelier, Small Methods 2019, 3, 1800218.

FUNCTIONA ___ MATERIALS

www.advancedsciencenews.com www.afm-journal.de

- [35] Z. Zou, Y. Mu, M. Han, Y. Chu, J. Liu, K. Zheng, Q. Zhang, M. Song, Q. Jian, Y. Wang, Energy Environ. Sci. 2025, 18, 2216.
- [36] G. Kresse, J. Furthmüller, Comput. Mater. Sci. 1996, 6, 15.
- [37] J. P. Perdew, K. Burke, M. Ernzerhof, *Phys. Rev. Lett.* **1996**, *77*, 3865
- [38] H. J. Monkhorst, J. D. Pack, Phys. Rev. B 1976, 13, 5188.
- [39] S. L. Dudarev, G. A. Botton, S. Y. Savrasov, C. Humphreys, A. P. Sutton, Phys. Rev. B 1998, 57, 1505.
- [40] K. A. Papadopoulou, A. Chroneos, S.-R. G. Christopoulos, Comput. Mater. Sci. 2022, 201, 110868.
- [41] H. Chen, S. Adams, IUCrJ 2017, 4, 614.
- [42] T. Aschebrock, S. Kümmel, Phys. Rev. Res. 2019, 1, 033082.
- [43] D. Gehringer, M. Friák, D. Holec, Comput. Phys. Commun. 2023, 286, 108664
- [44] A. Zunger, S.-H. Wei, L. G. Ferreira, J. E. Bernard, Phys. Rev. Lett. 1990, 65, 353.